Reverse Engineering of Feedforward Cortical-Hippocampal Neural Networks Relevant for Preclinical Disease Modelling

Katrine Sjaastad Hanssen*[1,2,✉], Nicolai Winter-Hjelm*[1,✉], Salome Nora Niethammer[1,2], Asgeir Kobro-Flatmoen[2,3], Menno P. Witter[2,3], Axel Sandvig[1,4], and Ioanna Sandvig*[1,✉]

[1]Department of Neuromedicine and Movement Science, Faculty of Medicine and Health Sciences, Norwegian University of Science and Technology (NTNU), Norway
[2]Kavli Institute for Systems Neuroscience, Centre for Neural Computation, Egil and Pauline Braathen and Fred Kavli Centre for Cortical Microcircuits, NTNU, Norway
[3]K.G. Jebsen Centre for Alzheimer's Disease, Faculty of Medicine and Health Sciences, NTNU, Norway
[4]Department of Neurology and Clinical Neurophysiology, St Olav´s University Hospital, Trondheim, Norway

Engineered biological neural networks are indispensable tools for investigating neural function in both healthy and diseased states from the subcellular to the network level. Neurons *in vitro* self-organize over time into networks of increasing structural and functional complexity, thus maintaining emergent dynamics of neurons in the brain. While *in vitro* neural network model systems have advanced significantly over the past decade, there is still a need for models able to recapitulate topological and functional organization of brain networks. Especially relevant in this context are interfaces which can support the establishment of multinodal interconnected networks of different neural populations, which at the same time enable control of the direction of connectivity between the nodes. An added required feature of such interfaces is compatibility with electrophysiological techniques and optical imaging tools to facilitate studies of neural network structure-function dynamics. In this study, we applied a custom-designed microfluidic device with Tesla-valve inspired microchannels for structuring multinodal neural networks with controllable feedforward connectivity between rat primary cortical and hippocampal neurons. By interfacing these devices with nanoporous microelectrode arrays, we demonstrate how both spontaneously evoked and stimulation induced activity propagates, as intended, in a feedforward pattern between the different interconnected neural nodes. Moreover, we show that these multinodal networks exhibit functional dynamics suggestive of capacity for both segregated and integrated activity. To advocate the broader applicability of this model system, we also provide proof of concept of long-term culturing of subregion- and layer specific neurons extracted from the entorhinal cortex and hippocampus of adult Alzheimer´s-model mice and rats. We show that these neurons re-form structural connections and develop spontaneous spiking activity after 15 days *in vitro*. Our results thus highlight the suitability and potential of our approach for reverse engineering of biologically and anatomically relevant multinodal neural networks supporting the study of dynamic structure-function relationships in both healthy and pathological conditions.

Advanced modelling | Self-organization | In vitro | Microfluidic Device | Electrophysiology | Cortex | Entorhinal cortex | Hippocampus | Adult neural networks | Alzheimer's model animals |

Correspondence: ***katrine.s.hanssen@ntnu.no | nicolai.winter-hjelm@ntnu.no | ioanna.sandvig@ntnu.no***
These authors share first authorship

Introduction

Engineered biological neural networks facilitate the study of dynamic properties of network structure and function at the micro- and mesoscale in highly controllable experimental conditions. There is compelling evidence that neurons *in vitro* maintain their inherent self-organizing properties and over time form neural networks with complex structure and function, thus recapitulating fundamental behaviour of brain networks (1–3). As such, engineered neural networks offer an complementary approach to *in vivo* studies for investigations of neural structure and function from the subcellular to the network level. In recent years, several methodological and technological developments have enabled advanced neural network modelling *in vitro* using microfluidic devices to engineer multinodal neural networks (4, 5). However, most studies to date are typically limited to using two-nodal microfluidic devices (6, 7). Thus, the potential of such neuroengineering approaches to recapitulate anatomically relevant network configurations Reis still underutilised. Additionally, the models tend to be limited in terms of their reproducibility, scalability, and adaptability especially in terms of being able to support multi-nodal, directional topological configurations resembling *in vivo* neural assemblies.

A key determinant for establishing anatomically relevant neural network configurations *in vitro* is facilitation and control of multi-nodality. Neural assemblies in the brain are structured into highly specialized functional regions connected through precise afferent-efferent axonal pathways, aiding feedforward and/or feedback signal propagation between pre- and postsynaptic nodes (8). During neural development in the brain, such directional projection sequences are established by finely tuned spatiotemporally regulated molecular and chemical guidance cues regulating axon growth and guidance (9–11). Such gradients are absent in an *in vitro* microenvironment, and alternative approaches are required to facilitate establishment of directional projections between the neural nodes. Several recent studies, including studies from our group, have demonstrated that directional axonal outgrowth between interconnected nodes can be achieved and controlled by embedding geometrical constraints within the microchannel architecture in microfluidic interfaces (12–20). Such models support control of connectivity between multiple neural subpopulations with high precision, rendering them especially interesting in the context of recapitulating anatomically relevant neural networks (21–24). By interfacing such microfluidic devices with microelectrode arrays (MEAs), emerging structure-function dynamics can also be studied electrophysiologically (25). Previous studies suggest that containment of neural networks into modular configurations can promote the development of a broader repertoire of activity dynamics compared to unstructured networks, akin

to complex information processing seen *in vivo* (22). For instance, we and others have shown that structurally coupled neural networks exhibit functional asymmetry, with independently regulated information processing within the interconnected nodes, as well as controlled information flow between them (20, 21, 26, 27).

A relevant neural network configuration to study using such interfaces is the highly interconnected entorhinal-hippocampal network, a brain area important for processing and storage of memories (28). This entorhinal-hippocampal network consists of multiple subregion specific cell types connected through axonal projections. Multinodal microfluidic devices offer an opportunity to reconstruct this network, and to study ongoing structural and functional dynamics in a highly controlled microenvironment. Furthermore, the entorhinal-hippocampal network is particularly vulnerable to Alzheimer's disease (AD), evidenced by early accumulation of tau pathology (29), amyloid-beta plaque load (30), altered neuronal activity in form of seizure-like hyperactivity (31), and major neuronal (32, 33) and synaptic loss (34, 35). Thus, this network is of high interest to study at preclinical stages of AD. We and others have demonstrated that adult entorhinal and hippocampal subregion specific cells from AD model mice are able to reconnect in culture (36–38). We also recently reported a method for long-term (>2 months) culturing and recording of lateral entorhinal cortex layer II (LEC LII) neurons from AD model animals *in vitro* (39). To our knowledge, culturing layer and subregion specific entorhinal-hippocampal neurons from AD model animals in multinodal microfluidics has however not been demonstrated.

In this study, we demonstrate reverse engineering of anatomically relevant biological neural networks, including layer specific neurons derived from adult AD model animals, using custom-designed microfluidic MEA interfaces. By incorporating Tesla-valve inspired microchannels, we can structure multi-nodal neural networks with controllable feedforward connectivity, and record spontaneously evoked and stimulation induced signal propagation in a feedforward pattern between the nodes. This engineering approach supports longitudinal study of dynamic structure-function relationships in both healthy and diseased neural networks with high temporal and spatial precision. Moreover, we demonstrate long-term culturing of region and layer specific neurons extracted from adult AD-model mice and rats on the platforms, in an anatomically relevant configuration. We show that these adult neurons re-form structural connections, and develop spontaneous electrophysiological spiking activity after 15 days *in vitro*. As such, we provide proof of concept for future applications of this model system for advanced preclinical disease modelling.

Materials and Methods

Experimental Design. An experimental timeline including a schematic of the microfluidic MEA design can be seen in **Figure 1**. Our neural cultures comprised either commercially available rat embryonic cortical and hippocampal neurons (hereafter referred to as cortical-hippocampal networks), or lateral entorhinal cortex layer II neurons (LEC-LII), Dentate Gyrus granular neurons (DG-gl), CA3 pyramidal neurons (CA3-pyr) and CA1 pyramidal neurons (CA1-pyr) freshly dissected from adult McGill-R-Thy1-APP AD-model rats or APP/PS1 AD-model mice (hereafter referred to as adult entorhinal-hippocampal AD networks). The method for the dissection and culturing of adult hippocampal neurons was refined from our previously reported protocol for adult lateralmost LEC LII (lLEC-LII) neurons from APP/PS1 model mice (39). For all cultures, coating and establishment of an astrocytic feeder layer was conducted using the same protocol.

Design & Fabrication of Microdevices. The four-nodal microdevices were designed using Clewin 4 (WieWeb Software, Enschede). Each node was $5\,\mathrm{mm}$ in diameter and $60\,\mu\mathrm{m}$ high. Furthermore, the nodes were connected by 20 microchannels. To induce unidirectional axonal outgrowth between the nodes, a geometrical design inspired by the Tesla-valve was implemented within the microchannel architecture (20). All channels were $350\,\mu\mathrm{m}$ long, $10\,\mu\mathrm{m}$ wide and $5\,\mu\mathrm{m}$ high. The design also had spine structures on the postsynaptic side to misguide axons trying to enter the microchannels. 49 nanoporous platinum electrodes of $50\,\mu\mathrm{m}$ diameter were positioned evenly spread across the four nodes. Additionally, 9 electrodes were positioned within the microfluidic channels to confirm active connections between the nodes. A reference electrode was split between all four chambers for enhanced signal-to-noise ratio. The design, as well as an image of a fabricated microdevice can be seen in **Figure S1**. Fabrication of all microdevices was conducted according to our recently reported protocol (20).

Animals Models and Genotyping. All animal experiments comply with the ARRIVE guidelines (40), were approved by the Norwegian Food Safety Authority and carried out in accordance with the EU (European Union) Directive 2010/63/EU for animal experiments. The animals were held in standard lab cages (up to 5 animals per cage), with temperatures of $22 \pm 2\,^{\circ}\mathrm{C}$, and kept at a light/dark cycle of 12:12 hours, with access to food and water *ad libitum*. We used a total of 43 adult McGill-R-Thy1-APP rats, including female (n=22) and male (n=21), and a total of 2 female, adult APP/PS1 mice. See **Supplementary Table S2** for a total overview of sex, age and genotype of all animals.

The APP/PS1 mouse model is a transgenic familial AD-model, with a C57BL/6J genetic background, co-expressing mutated human amyloid precursor protein (hAPP) (KM670/671NL) and mutated human presenilin 1 (L166). Both mutated proteins are driven by expression cassettes under the Thy1 promoter. This causes increased levels of Aβ leading to formation of extracellular cortical Aβ-deposits starting already from around 6 weeks of age (41). The APP/PS1 mice were genotyped using a KAPA-kit as described in Hanssen *et al.* (39). The McGill-R-Thy1-APP rat model is a transgenic familial AD model with a Wistar (Hsd-Brl:WH) genetic background, co-expressing mutated hAPP (APP K670M671delinsNL) and (APP V717F) (42). The

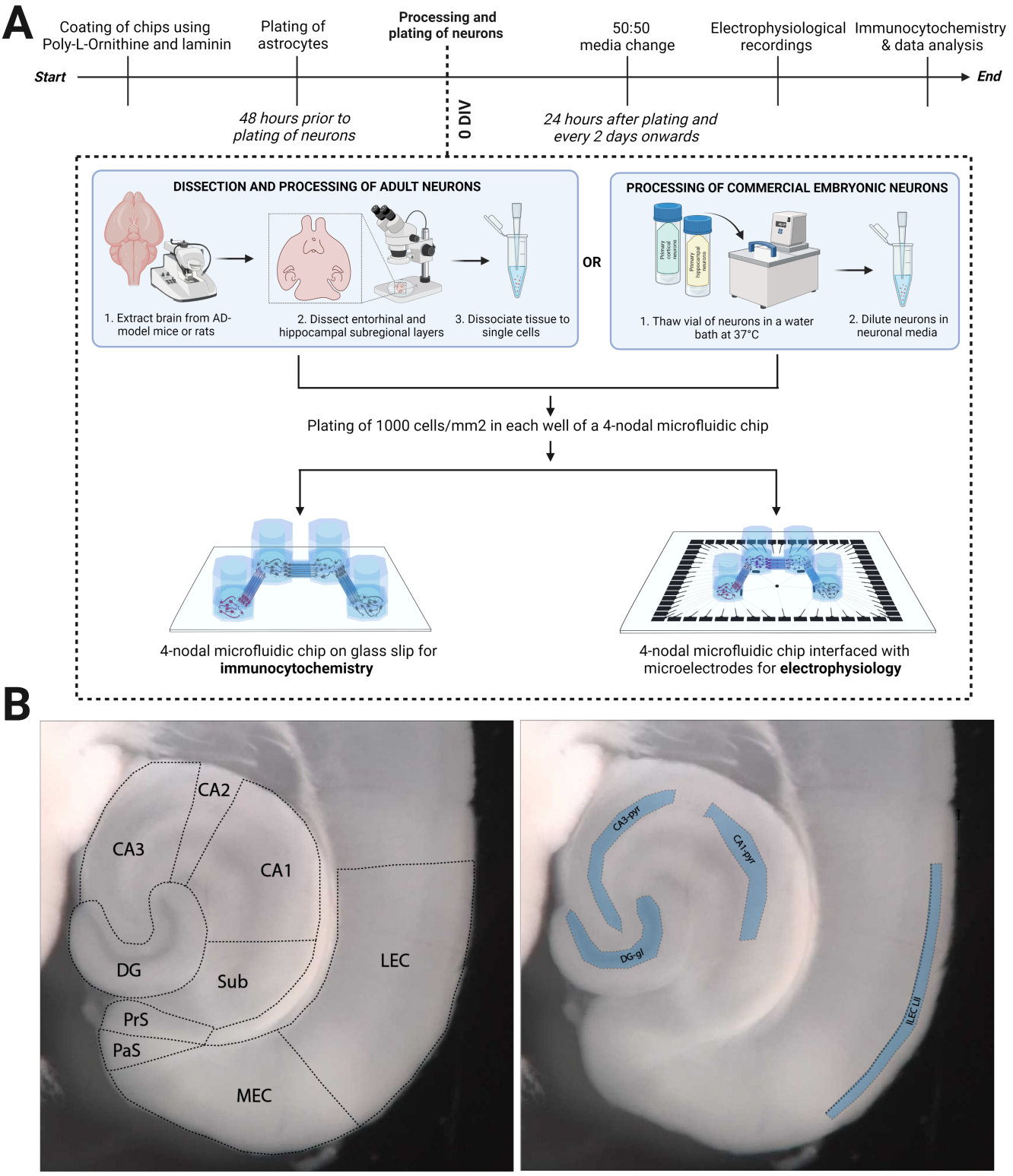

Figure 1 | **Experimental timeline. (A.)** Microfluidic chips were coated with Poly-L-Ornithine and laminin prior to plating of rat cortical astrocytes. On day 0, brains of adult mice and rats were extracted and horizontally sectioned before dissection of the lateral entorhinal cortex layer II, and hippocampal subregional layers (dentate gyrus granular layer, and CA3- and CA1 pyramidal layers). Dissected entorhinal and hippocampal tissue were furthermore dissociated into single cells enzymatically and manually by trituration. Commercial embryonic rat cortical and hippocampal primary neurons were collected from a nitrogen tank and immediately thawed in a water bath at $37\,^{\circ}\mathrm{C}$. The cortical-hippocampal and adult entorhinal-hippocampal neurons were plated at a density of 750 and $1000\,\mathrm{cells/mm^2}$ in each well of a four-nodal microfluidic chip, respectively. For the adult cultures, LEC LII, DG-gl, CA3-pyr and CA1-pyr were plated in nodes 1-4, respectively. For the embryonic cultures, cortical neurons were plated in node 1, and hippocampal neurons in nodes 2-4. These devices were interfaced with glass coverslips or microelectrode arrays. **(B.)** A horizontally cut brain section viewed under a stereoscope using fiber optic lamps for contrast with delineation of entorhinal and hippocampal subregions (left). Lateral entorhinal cortex layer II (LEC LII) and hippocampal dentate gyrus granular layer (DG-gl), CA3 pyramidal layer (CA3-pyr) and CA1 pyramidal layer (CA1-pyr) highlighted in blue. Figure created in BioRender.com.

McGill-R-Thy1-APP rats were genotyped using quantitative PCR (qPCR) and genomic DNA isolated from ear tissue as described in previous studies (43, 44).

Cell Experiments and Models.

Coating of Culturing Platforms. Prior to coating, all microdevices were sterilized in UV light over night in a biosafety cabinet. Consecutively, the distilled (DI) water in the devices was replaced by Poly-L-Ornithine solution (PLO) (Sigma-Aldrich, A-004-C) at a concentration of $0.1\,\mathrm{mg/mL}$ and incubated at $37\,^{\circ}\mathrm{C}$, $5\,\%$ CO_2 for $2\,\mathrm{h}$ *or* overnight at $4\,^{\circ}\mathrm{C}$. Subsequently, all PLO was discarded and the microdevices rinsed three times for $10\,\mathrm{min}$ with milli-Q (MQ) water. After the last rinse, laminin solution consisting of $16\,\mu\mathrm{g/mL}$ natural mouse laminin (Gibco™, 23017015) in phosphate-buffered saline (PBS, Sigma-Aldrich, D8537) was added and the microdevices incubated at $37\,^{\circ}\mathrm{C}$, $5\,\%$ CO_2 for $2\,\mathrm{h}$. A hydrostatic pressure gradient was established during all coating to ensure flow of the coating solution through the microchannels. This was achieved by filling the chambers with an unequal amount of coating solution.

Seeding of Astrocyte Feeder Layer. For the astrocytic feeder layer, a solution consisting of DMEM, low glucose (Gibco™, 11885084) supplemented with $15\,\%$ Fetal Bovine Serum (Sigma-Aldrich, F9665) and $2\,\%$ Penicillin-Streptomycin (Sigma-Aldrich, P4333) was prepared. Next, the coating solution was replaced by the astrocyte media, and rat cortical astrocytes (Gibco™, N7745100) were seeded at a density of $100\,\mathrm{cells/mm^2}$, i.e., 2000 cells per microchamber. The astrocytes were allowed to expand for $48\,\mathrm{h}$, before seeding of either embryonic cortical and hippocampal neurons or adult entorhinal and hippocampal neurons.

Embryonic Neurons: Plating and Maintenance. Neural media consisting of Neurobasal Plus Medium (Gibco™, A3582801) supplemented with $2\,\%$ B27+ (Gibco™, A358201), $1\,\%$ GlutaMax (Gibco™, 35050038) and $2\,\%$ Penicillin-Streptomycin (Sigma-Aldrich, P4333) was prepared. Rock Inhibitor (Y-27632 dihydrochloride, Y0503, Sigma-Aldrich) was additionally added to the media during the first two days of neural growth at a concentration of $0.1\,\%$ to increase neural survival. Rat cortical neurons from Sprague Dawley rats (Gibco, A36511) were plated at a density of $1000\,\mathrm{cells/mm^2}$, equalling 20 000 cells in the first node. The cortical neurons were thereafter allowed to settle in an incubator for $3\,\mathrm{h}$ before plating the hippocampal neurons. Next, rat hippocampal neurons from Sprague Dawley rats (Gibco, A36513) were plated at a density of $1000\,\mathrm{cells/mm^2}$ in the three remaining nodes. Half the neural media was replaced with fresh neural media 4 hours after plating, and again after $24\,\mathrm{h}$. From here on, half the neural media was replaced every second day throughout the experimental period.

Adult Neurons: Dissection. All tools were sterilized by autoclaving before use. Both mice and rats were deeply anesthetized using $5\,\%$ isoflurane gas (Abbott Lab, 05260–05) and checked for absence of reflexes before the head was decapitated with a guillotine for rats or surgical scissors (FST, 14007–14) for mice. Subsequently, dissection and sectioning of the brain were conducted as described previously for both mice and rats (39) where a full detailed description of the procedure can be found. Brains were extracted in a petri dish filled with Hanks Balanced Salt Solution (Thermo Fischer Scientific, 88284) kept on ice. Extracted brains were sectioned horizontally on a vibratome (thickness of $300\,\mu\mathrm{m}$, frequency of $5.3\,\mathrm{Hz}$ and speed of $8\,\mathrm{mm/s}$) with $0.2\,\%$ AGAR (VWR, 20767.298) supporting the caudal end of the brain. Sectioned brain slices were immediately transferred to wells of a sterile 24-well plate held on ice. Sections were further transferred to a petri dish held on ice and viewed under a stereoscope with fiber optic lamps, allowing for sufficient contrast of the cytoarchitechtonic landmarks. Dissection of the lateral entorhinal cortex layer II (LEC-LII) was conducted as described in our recent study for both mice and rats (39). Additionally, the dentate gurys granular layer (DG-gl), CA3 pyramidal (pyr) and CA1-pyr layers were dissected (see **Figure 1B**). The DG-gl can be separated from the molecular layer and hilus with its densely packed layer of granular neurons (45). Similarly, the pyramidal layer in CA3 and CA1 consists of densely packed pyramidal neurons (46) that can be distinguished from deeper layers lucidum, radiatum and stratum locus molecular and superficial layer oriens (28). All dissected strips of tissue were placed by region in four separate sterile $15\,\mathrm{mL}$ tubes filled with dissection media (HABG-P) consisting of Hibernate-A (Thermo Fischer Scientific, A1247501) supplemented with $2\,\%$ B27+ (Gibco™, A3582801), $2.5\,\%$ GlutaMAX (Gibco™, 35050061) and $1\,\%$ Penicillin-streptomycin (Sigma-Aldrich, P4333), placed on ice.

Adult Neurons: Plating and Maintenance. All dissected tissue was rinsed for debris three times by adding and removing $3\,\mathrm{mL}$ of HABG-P. Following this, all media was discarded and the tissue was dissociated for $15\,\mathrm{min}$ at $37\,^{\circ}\mathrm{C}$, $5\,\%$ CO_2, $20\,\%$ O_2 in Neural Isolation Enzyme Papain (Thermo Fischer Scientific, 88285) reconstituted in Hank's Balanced Salt solution (Thermo Fischer Scientific, 88284) as described by the manufacturer (Thermo Fischer Scientific, MAN0011896). Subsequently, all dissociation enzyme was discarded, $100\,\mu\mathrm{L}$ HABG-P was added and the tissue was manually triturated 10 times by using a $100\,\mu\mathrm{L}$ pipette tip. Further, all HABG-P was topped up to a total of $3\,\mathrm{mL}$ and the vials of tissue were centrifuged at x200 g for $2\,\mathrm{min}$ in room temperature. After centrifugation, all HABG-P was discarded and $100\,\mu\mathrm{L}$ neural media was added before manual trituration 10 times using a $100\,\mu\mathrm{L}$ pipette tip. Neural media consisting of Neurobasal Plus Medium (Gibco™, A3582801) supplemented with $2\,\%$ B27+ (Gibco™, A358201), $1\,\%$ GlutaMax (Gibco™, 35050038), $2\,\%$ Penicillin-Streptomycin (Sigma-Aldrich, P4333), $0.1\,\%$ Rock Inhibitor (Y-27632 dihydrochloride, Y0503, Sigma-Aldrich) and $10\,\%$ Fetal Bovine Serum (Sigma Aldrich, 12106C). For adult neurons derived from mice, $0.1\,\%$ BDNF (Neurotrophins, 450-02) was added to the neural media. For adult neurons derived

from rats, 0.1 % FGF2 (Thermo Fisher Scientific, 13256-029) was added to the neural media. We plated the neurons at a total density of 750 cells/mm^2, equalling 15 000 cells in each node of the microfluidic chip. Half the neural media was replaced every second day throughout the experimental period.

Immunocytochemistry. For immunocytochemistry, both cortical-hippocampal and adult entorhinal-hippocampal neurons were plated in microfluidic platforms bonded to glass coverslips (VWR International, 24x24 mm No. 1 Menzel-Gläser). Fixation of cortical-hippocampal cultures was conducted using glyoxal solution based on the protocol by Richter *et al.* (47). This fixative consisted of 71 % MQ water, 20 % ethanol absolute (Kemetyl, 100 %), 8.0 % Glyoxal solution (Sigma-Aldrich, 128465) and 1 % acetic acid (Sigma-Aldrich, 1.00063). Fixation of adult entorhinal-hippocampal cultures was conducted using PBS (Sigma-Aldrich, D8537) containing 0.4 M phosphate buffer and 4 % freshly depolymerized paraformaldehyde (PFA; Sigma-Aldrich, P6148). The cultures were washed with PBS to remove debris, before the fixative was applied for 15 min at RT. Subsequently, all chambers were washed with PBS 3 times for 15 min each. Next, 0.5 % Triton-X (Sigma-Aldrich, 1086431000) diluted in PBS was applied to permeabilize the cells. All chambers were again washed twice with PBS before a blocking solution consisting of 5 % goat serum (Abcam, ab7481) diluted in PBS was added to the cultures, and the cultures incubated at room temperature on a shaking table at 30 rpm for 1 h. Primary antibody solutions were prepared in PBS with 5 % goat serum, and antibody concentrations according to the ones listed in **Table 1**. Cultures were placed on a shaker table at 30 rpm at 4 °C overnight. Following, the primary antibody solution was removed, and the cell cultures were rinsed three times with PBS for 15 min each. Next, a secondary antibody solution consisting of 0.2 % secondaries and 5 % goat serum diluted in PBS was added to the cultures. The cultures were left to rest on a shaker table at 30 rpm for 3 h at RT. Prior to applying the secondary antibody solution, the prepared solutions were centrifuged at 6000 rpm for at least 15 min to remove precipitates. Subsequently, the secondary antibody solution was replaced by Hoechst (Abcam, ab228550) at a concentration of 0.1 % diluted in PBS, and the cultures left on a shaker table for another 30 min. Eventually, all cultures were washed three more times in PBS, then twice in MQ water prior to imaging.

Table 1 | Antibodies and concentrations used for Immunocytochemistry.

Marker	Catalogue Number	Concentration
β3-Tubulin	Ab78078	1/1000
GAP-43	9264 (Sigma-Aldrich)	1/500
GFAP	Ab7260	1/1000
MAP2	Ab5392	1/5000
NeuN	Ab279295	1/500
Neurofilament Heavy	Ab4680	1/5000
Reelin	Ab78540	1/10000

All antibodies were purchased from Abcam unless otherwise stated.

All images were acquired using an EVOS M5000 microscope (Invitrogen). The microscope was equipped with DAPI (AMEP4650), CY5 (AMEP4656), GFP (AMEP4651) and TxRed (AMEP4655) LED light cubes and Olympus UPLSAP0 4X/0.16 NA and 20x/0.75 NA objectives. Post-processing of images was conducted in ImageJ/Fiji or Adobe Photoshop 2020.

Imaging and Quantification of Neurite Length. For quantification of neurite length, phase contrast images acquired using a Zeiss Axio Vert V.1 brightfield 20x/53 WD/0.4 NA objective with an Axiocam 202 mono were used. For analysis, Neurolucida was used to quantify neurite length of the adult neurons.

Electrophysiology and Data Analysis.

Electrophysiological Recordings. A MEA2100 workstation (Multichannel Systems) was utilized for all recordings with a sampling rate of 25 000 Hz. An external temperature controller (TC01, Multichannel Systems) was used to maintain the temperature at 37 °C. All cultures were allowed to equilibrate at the workstation for 5 min prior to recordings, and recordings lasted for 15 min for cortical-hippocampal cultures and 10 min for adult entorhinal-hippocampal neural networks. A 3D-printed plastic cover with a gas-permeable membrane was used to keep cultures in a sterile environment during the recordings.

Electrical Stimulations. Stimulations were performed for the cortical-hippocampal neurons following the recordings at 28 and 32 DIV using a train of 60 spikes at $\pm$ 800 mV (positive phase first) of 200 µs duration with an inter-spike interval of 5 s. The most active electrode measured in spikes per second in the cortical cell population was chosen for stimulations. This was done to assure that the electrode chosen for stimulation had sufficient coupling with a neuron to induce activity.

Data Analysis. All data preprocessing and analysis was conducted in Matlab R2021b, and graphs were plotted using the matlab function linspecer (48), based on the color palette colorBrewer (49). A 4th order Butterworth bandpass filter was used to remove noise below 300 Hz and above 3000 Hz, and a notch filter to remove noise at 50 Hz from the power supply mains. All filters were run using zero-phase digital filtering. For spike detection, the Precise Timing Spike Detection (PTSD) algorithm developed by Maccione *et al.* (50) was utilized. A threshold of 9 times the standard deviation was chosen for the cortical-hippocampal cultures, with a maximum peak duration of 1 ms and a refractory periode of 1.6 ms. For the adult entorhinal-hippocampal cultures, a standard deviation of 7.5 was chosen due to the lower signal-to-noise ratio of the activity in these cultures overall. The SpikeRasterPlot function developed by Kraus (51) was adapted and used for creating raster plots.

Burst detection was conducted using the logISI algorithm developed by Pasquale *et al.* (1). A minimum of four consecutive spikes was set as a hard threshold for a burst to be detected, and the maximum inter-spike interval to 100 ms. Net-

work bursts were detected using the logIBEI approach (52), with a minimum of 10 % of all active electrodes required to exhibit bursting activity for a network burst to be classified.
After binning the data into 50 ms time bins, functional connectivity was analysed using Pearson correlation. Intranodal correlation was evaluated by taking the average correlation of all active connections within each node. Internodal correlation was evaluated by taking the correlation between the summed activity of all four nodes in the four-nodal network.
To visualize key network features, graphs were plotted using the functional connectivity as edges between the individual nodes (herein representing the individual electrodes). Firing rate (Hz) was furthermore used to represent the node color, betweenness centrality the node size and node edge color the community belonging. Graph theoretical measures were calculated using the Brain Connectivity Toolbox developed by Rubinov & Sporns (53), from which the Louvain algorithm was used to perform community detection (54).
To remove stimulation artifacts, stimulation data was run through the SALPA filter developed by Wagenaar *et al.* (55). Additionally, 15 ms of the filtered data was blanked following each stimulation time point. Subsequently, the data was binned into 20 ms time bins, and peristimulus time histograms of the average response of the stimulations in each node plotted.

Results

Establishment of Feedforward Cortical-Hippocampal Networks. In this study, we reverse engineered multi-nodal rodent cortical-hippocampal neural networks with controllable afferent-efferent connectivity using custom-designed microfluidic devices interfaced with microelectrode arrays. We found that neurites from presynaptic nodes started entering the microchannels within the first week after plating, while axonal bundles could be observed crossing the microchannels between all nodes as early as 14 DIV (**Figure 2A**). At this timepoint, electrophysiological recordings indicated that spontaneous neural activity had already started transitioning from immature tonic firing to synchronous bursting within the nodes, consistent with previous findings (1, 2, 20, 56, 57). Representative graphs of both bursting activity and individual spikes within the cortical and hippocampal nodes can be seen in **Figure 2B**.
Both spontaneously evoked and stimulation induced network bursts were used to assess the capacity of the networks for feedforward activity propagation between the four unidirectionally connected nodes. All four nodes exhibited bursting activity already at 12 DIV, and the burst rate increased steadily with time (**Figure 2C**). Until 20 DIV, bursts were mainly contained within the individual nodes, or spread between only a subset of the nodes. As the networks continued to mature, more bursts initiated in the cortical node could be seen spreading sequentially through all three hippocampal nodes. A 200 s representative raster plot of a multinodal cortical-hippocampal network at 28 DIV can be seen in **Figure 2D**, with the different nodes marked with different shades of blue. Observation of a typical network burst clearly shows how activity originating from the cortical node is spreading in a feedforward manner between all four interconnected nodes. Furthermore, electrical stimulation delivered to the cortical node initiated activity propagating sequentially between the four nodes, as seen in the peristimulus time histogram in **Figure 2E**. **Figure 2F** shows the percentage of all network bursts that were initiated within the cortical node and where either contained in the specific node, or spread to the next two or three nodes. The total number of network bursts detected during a typical recording is seen along the secondary y-axis. At 28 DIV, as much as 24.2 % of the network bursts propagated through all four nodes, compared to less than 2 % at 12 DIV. For comparison (at 28 DIV) 4.5 %, 13.4 % and 4.4 % of the network bursts that were initiated in the cortical node propagated and stopped after the first, second and third node, respectively. This indicated establishment of more mature directional projection sequences between the nodes. The remaining percentages of network bursts were initiated within the second, third or fourth node. Similar trends were found for the other five networks (see **Figure S2**).

Functional Integration Increases, While Functional Segregation is Maintained Over Time in Reverse Engineered Multinodal Neural Networks. The functional connectivity of the networks was evaluated using Pearson correlation. Both intranodal and internodal correlation increased over time. Correlation matrices showing the temporal development in functional connectivity for one representative network can be seen in **Figure 3A**. While some internodal correlation could be observed between nodes already at 12 DIV, integration of all neighboring nodes was not established until 20 DIV. At 28 DIV, a higher correlation was also seen between non-neighboring nodes, indicative of a higher network-wide synchronization at this point (20, 26, 27). The graph representation of the network seen in **Figure 3B** furthermore highlights this network-wide functional integration. It additionally shows how the internodal correlation is clearly strongest between neighboring nodes, while the intranodal correlation on average is higher than the internodal correlation.
Furthermore, the entire reverse-engineeered cortical-hippocampal network could be mathematically delineated into four distinct modules using the Louvain algorithm, represented as the node edge color in **Figure 3B**. The median modularity value stayed close to 0.6 for all networks throughout the experimental period, indicating that the networks retained functional segregation of the four nodes (**Figure 3C**).

Structural Maturation of Cortical-Hippocampal Networks. As we saw a high level of functional integration between the nodes beyond 20 DIV, we also evaluated the networks' structural maturation using immunocytochemistry. To do so, we stained cells in each of the four nodes for both developmental and mature cytoskeletal and nucleic markers at 27 DIV. High levels of Growth-Associated Protein 43 (GAP43) were expressed for both the cortical and hippocampal nodes at 27 DIV (**Figure 4A**). This marker was used

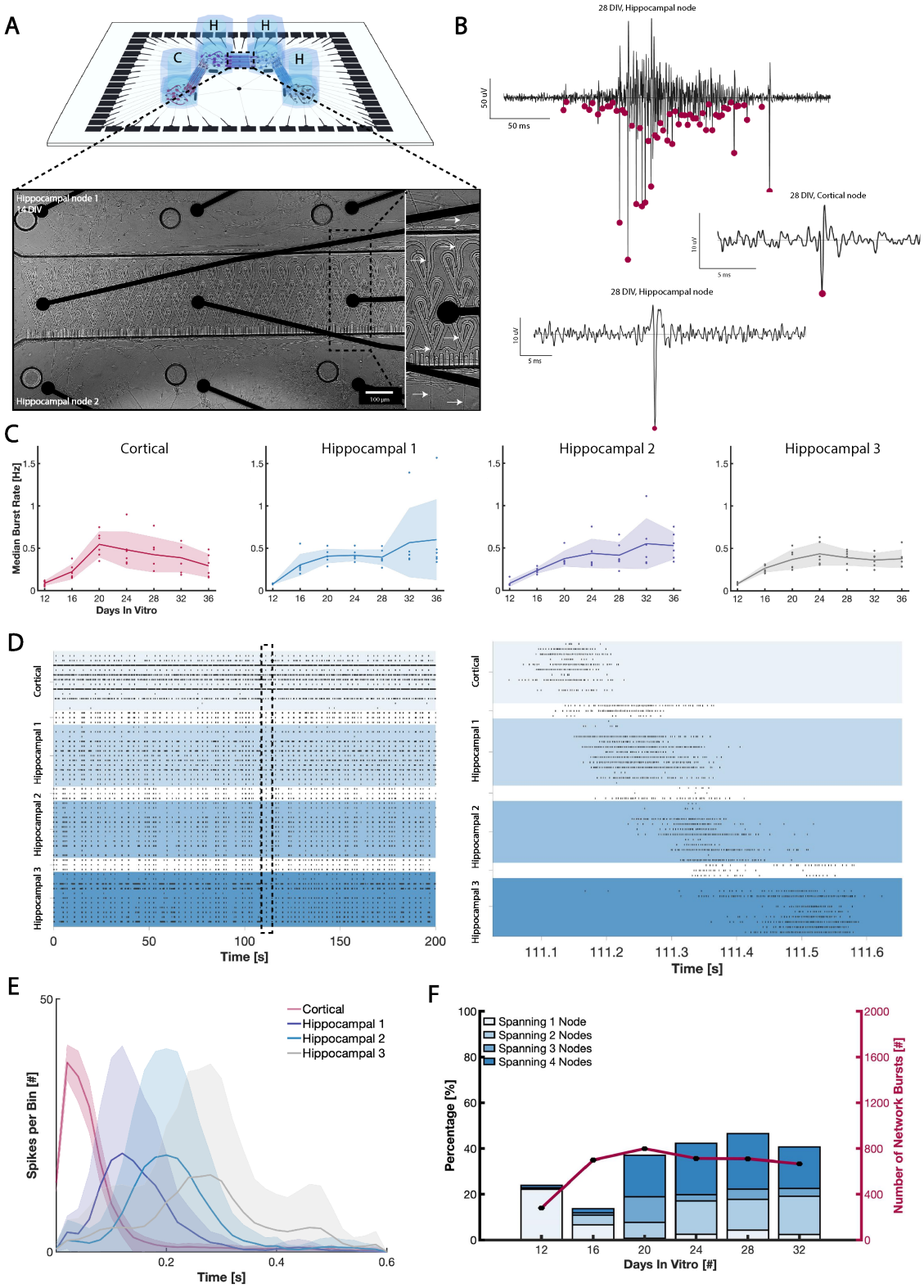

Figure 2 | **Feedforward activity propagation in the four-nodal cortical-hippocampal networks.** **(A.)** Representative micrograph of axons within the microchannels connecting two hippocampal nodes at 14 DIV. Examples of axonal bundles passing through microchannels (both with and without embedded microelectrodes) are highlighted with white arrows. **(B.)** Voltage traces showing a burst detected within one of the hippocampal nodes at 28 DIV, as well as representative examples of spikes detected within the cortical and hippocampal nodes. Pink specks represent spikes detected by the PTSD algorithm. **(C.)** Plots of the median burst rate for the four individual nodes. All nodes displayed an increasing burst rate until 20 DIV, at which point the rate started to flatten out. **(D.)** Representative raster plot showing the complex network dynamics emerging in the four-nodal cultures. A fraction of the network bursts were also clearly spreading from the cortical node throughout all four nodes, as represented in the zoomed-in graph. **(E.)** Peristimulus time histogram displaying the average response of each of the four nodes following repeated (n=60) stimulations of the cortical node for one network at 28 DIV. The stimulations clearly induced feedforward activity propagating throughout all four nodes. **(F.)** Histogram showing the percentage of spontaneously evoked network bursts initiated within the cortical population, and the number of nodes they spanned. The total number of network bursts initiated at each DIV is shown along the secondary y-axis.

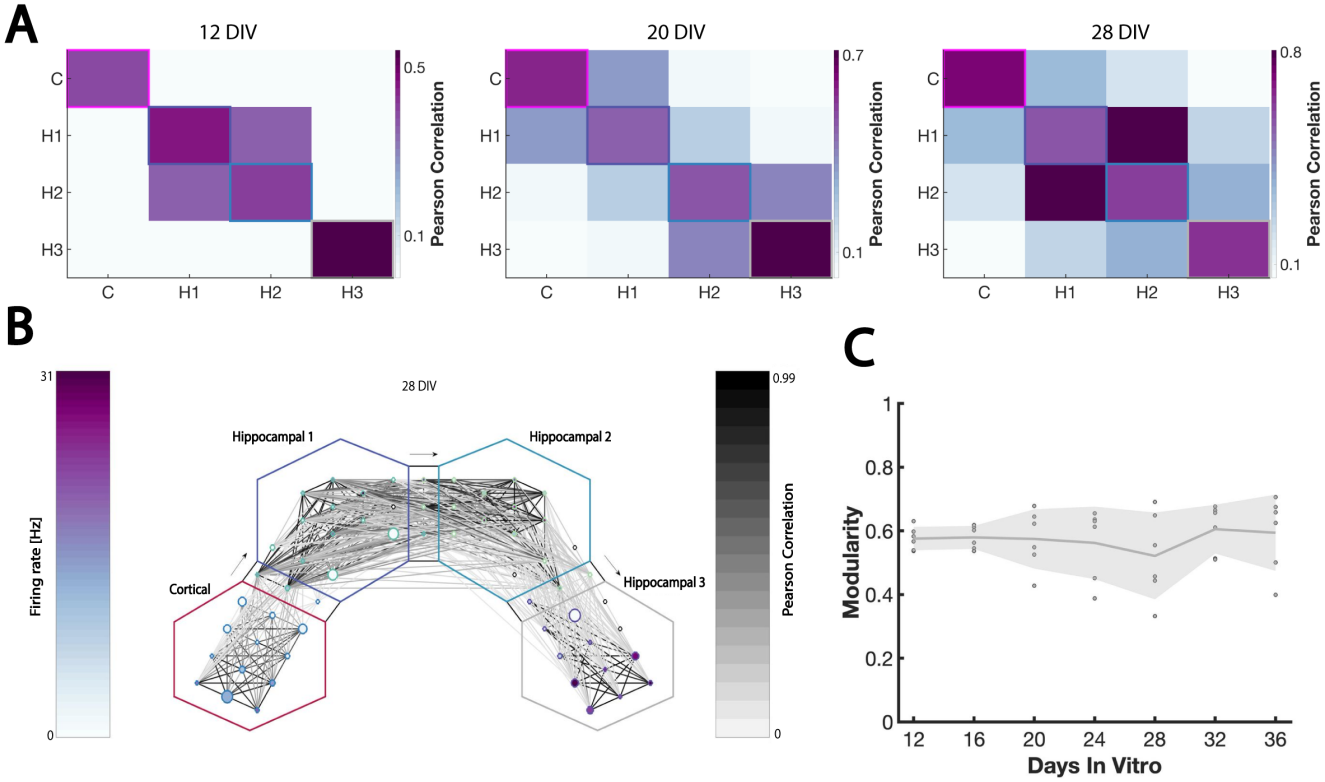

Figure 3 | **Functional connectivity of the cortical-hippocampal networks.** **(A.)** Correlation matrices showing the temporal increase in functional connectivity of one representative network over time from 12 DIV to 28 DIV. **(B.)** Representative graph of a single network at 28 DIV displaying individual electrodes as nodes and their correlation as edges. Node color represents firing rate, node size betweenness centrality and node edge color community belonging. As illustrated, the network can be clearly delineated into distinct communities, with higher intranodal than internodal functional connectivity. **(C.)** Modularity for the four-nodal networks, indicating a retained functional segregation over time.

in combination with the cytoskeletal proteins Microtubule-Associated Protein 2 (MAP2) and β3-Tubulin, which are expressed from early axiogenesis and onwards (58–62). As GAP43 is critical for neurodevelopment and growth cone migration, these expression levels indicate that structural changes were still evolving beyond three weeks *in vitro* (63). Furthermore, both Neural Nuclear Protein (NeuN) and Neurofilament Heavy (NFH) have been found to be specific for mature neurons, and were used here to assess the maturity of the engineered networks (**Figure 4B**) (64, 65). These markers were used in combination with the glial marker GFAP (66). We found all these proteins to be prominently expressed at 27 DIV, indicating that the networks were reaching structural maturity. This is also consistent with the findings from the electrophysiology, showing highly integrated dynamics between the nodes (**Figure 3**).

Adult Entorhinal and Hippocampal AD Neurons Reform Structural Networks and Exhibit Electrophysiological Activity. To further demonstrate the wider applicability of our model system for reverse engineering anatomically relevant networks for preclinical disease modelling, we used this system to culture neurons extracted from brain regions of interest from adult AD model animals. Our procedure to dissect and culture adult LEC LII neurons along with hippocampal DG-gr, CA3-pyr and CA1-pyr neurons from AD-model mice and rats is outlined in **Figure 1**. This method for the dissection and culturing of layer specific entorhinal and hippocampal neurons from AD model rats and mice builds upon our recently published method for extraction and culturing of LEC LII neurons from adult AD model APP/PS1 mice (39). We found that adult neurons from both AD model rats- (**Figure 5**) and mice (**Figure S4**) were able to re-form structural connections *in vitro*. Furthermore, we found that an astrocytic feeder layer was crucial for attachment of adult entorhinal and hippocampal AD neurons (**Figure S3A**), in line with our previous findings (39). Various combinations of neural media supplements were tested (**Table S1**), and neurites of adult rat neurons were found to significantly enhance their outgrowth when adding the growth factor FGF2 (10ng/mL) after 5 DIV (**Figure S3B & S3C**, all p-values for P3 < 0.01). Immunocytochemistry of our cultured adult neurons showed co-expression of neural marker NeuN and reelin in the LEC LII neurons, thus confirming regional identity, and co-expression of NeuN and Neurofilament Heavy for hippocampal DG-gr, CA3-pyr and CA1-pyr. This confirmed that the engineered network consisted of the neurons of interest (**Figure 6**). From 15 DIV, the networks started exhibiting spontaneous spiking activity (**Figure 7B** for rats, **Figure S5A** for mice). A raster plot showing that the neurons expressed sparse, desynchronized spiking activity with no bursts is seen in **Figure 7C**. Calculations of the median firing rate over time showed that the networks remained active up to at least 47 days *in vitro* (**Figure 7D**).

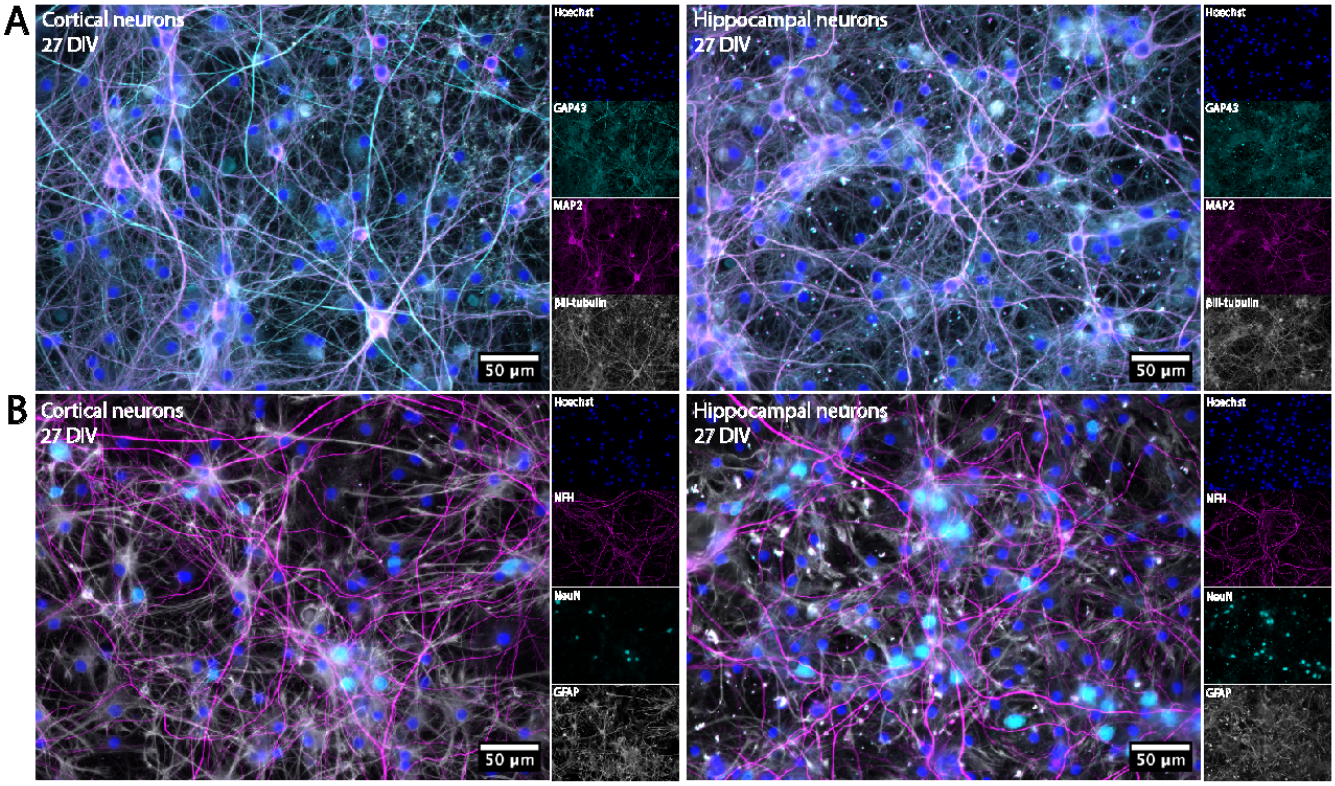

Figure 4 | **Immunocytochemistry of cortical-hippocampal networks. (A.)** Both cortical and hippocampal cultures self-organized into complex networks, as indicated by the cytoskeletal marker proteins β3-Tubulin and MAP2. The networks still underwent some level of self-organization and maturation at 27 DIV, as indicated by GAP43, a protein critical for neurodevelopment and growth cone migration. **(B.)** The networks had reached a high level of structural maturity at 27 DIV, indicated by the mature markers Neurofilament Heavy (NFH) and NeuN.

Discussion

In this study we have demonstrated reverse engineering of complex multi-nodal cortical-hippocampal neural networks with controllable afferent-efferent connectivity. We have furthermore illustrated the potential of this approach for advanced modelling of neural network function and dysfunction, by providing proof of concept of long-term culture of layer specific entorhinal-hippocampal networks from adult AD transgenic rats and mice.

Our engineered embryonic cortical-hippocampal networks recapitulated fundamental neural design principles by exhibiting spontaneous, complex structure-function dynamics over time. Specifically, these networks exhibited both segregated and integrated bursting activity across the four nodes (**Figure 2F**). Furthermore, electrical stimulations of the presynaptic, cortical node within these networks readily induced bursting activity that propagated sequentially, in a feedforward pattern, through the rest of the interconnected nodes (**Figure 2E**). The differences in number of nodes that network bursts spanned can be indicative of the networks' capacity for gating information, i.e. selectively transmitting only a subset of the information to other nodes (20, 21, 26, 27). Our results furthermore showed that the network modularity remained close to 0.6 for all networks throughout the experimental period. In comparison, in our previous study, we found the median modularity value to be 0.39 and 0.03 for two-nodal and one-nodal networks (20). As such, the four-nodal configuration of the present model system promoted efficient network organization, exhibited both integrated and segregated functional dynamics resembling those seen in neural networks *in vivo* (67–69).

The adult neural networks derived from AD model mice and rats exhibited electrophysiological spiking activity from 15 DIV (**Figure 7**). Spontaneously evoked neural activity was recorded, and a desynchronized firing pattern with no apparent bursting was observed (**Figure 7C**), in line with our recently reported findings from adult mouse LEC-LII neuron cultures (39). Additionally, previous studies performing patch-clamp recordings on cultured adult mouse hippocampal neurons have reported the neurons to exhibit activity as single spike events, rather than repetitive firing patterns (70, 71). A recent study also showed that both cortical and hippocampal neurons derived from adult wild-type mice expressed sparse bursting (<1 bursts per minute) (72). Furthermore, *ex vivo* whole-cell patch-clamp recordings from LEC LII neurons have shown that large depolarizing current-steps are necessary to elicit a burst in these neurons (73).

Advanced engineered interfaces as the ones demonstrated in this study can be particularly useful for modelling disease development and progression. The increasing body of literature on healthy development and maturation of neural networks *in vitro* aids in establishing baseline conditions for such studies. As previously described, healthy networks show a gradual transitioning from tonic, desynchronized intranodal fir-

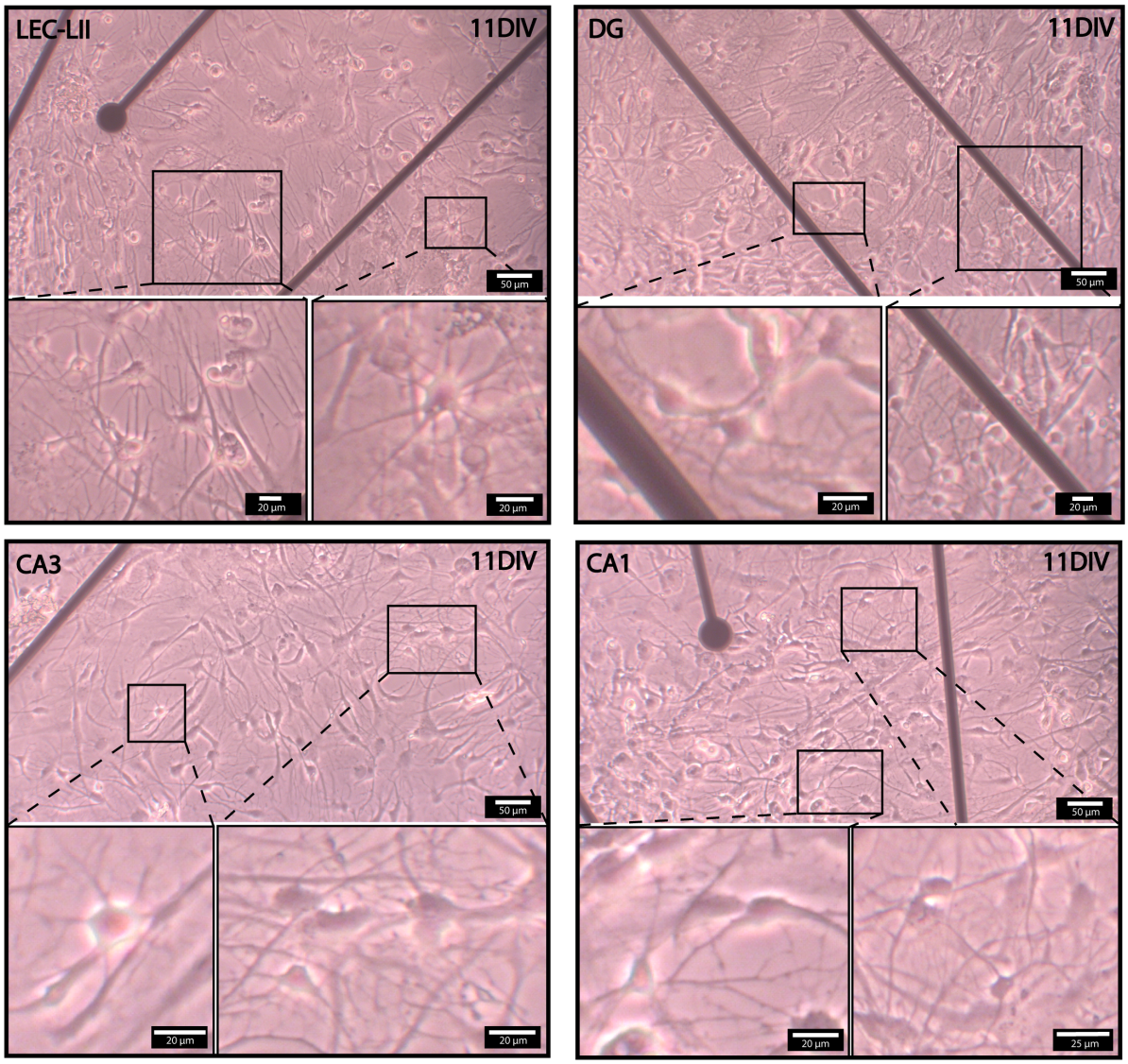

Figure 5 | Adult entorhinal and hippocampal AD neurons re-form structural connections *in vitro*. Phase-contrast images of adult neurons from LEC LII, DG, CA3 and CA1 at 11 DIV. Enlarged insets from all regions showing neural bodies with extruding neurites. Scalebars as indicated. LEC LII; lateral entorhinal cortex layer II. DG; denate gyrus. CA3/CA1; Cornu ammonis 3 and 1. DIV; days *in vitro*.

ing to network wide internodal integration of function during development (1, 2, 20, 57). Furthermore, they establish mature synaptic connections and an excitation-inhibition balance (20, 56). By comparing healthy networks to networks exhibiting pathological traits, such as the neurons from AD model animals used in this study, intra- and internodal changes in response to developing pathology can be modelled and studied. Such changes could for instance be hyperactivity in neurons surrounded by amyloid-β plaques (74) or changes in firing characteristics in form of decreased firing frequency (75). A critical risk factor for several neurodegenerative diseases and disorders, including AD, is also age. To accurately model disease development and progression, using cells from adult animals can as such have an impact on structural and functional dynamics due to the variations in epigenetic profile between embryonic and adult cells. The division of the distinct neural subpopulations into separate nodes can additionally support studies of propagation of pathological processes from pre- to postsynaptic nodes, further expanding on previous findings from our group (76). The ability to model such processes is highly relevant for elucidation of disease mechanisms, as well as identification of potential time windows and modes of therapeutic intervention.

Neural microcircuits in the brain, such as the entorhinal-hippocampal network, are profoundly complex systems with an intricate microarchitecture involving distinct subpopulations of neurons and other cells. Capturing the full complexity of such microarchitectures *in vitro* is per definition beyond the scope of reverse engineering approaches. Nonetheless, the present study clearly illustrates the robustness and potential of advanced neuroengineering in recapitulating complex network dynamics *in vitro*, and as such, it builds upon and expands on previous work (20, 21, 57, 76–79).

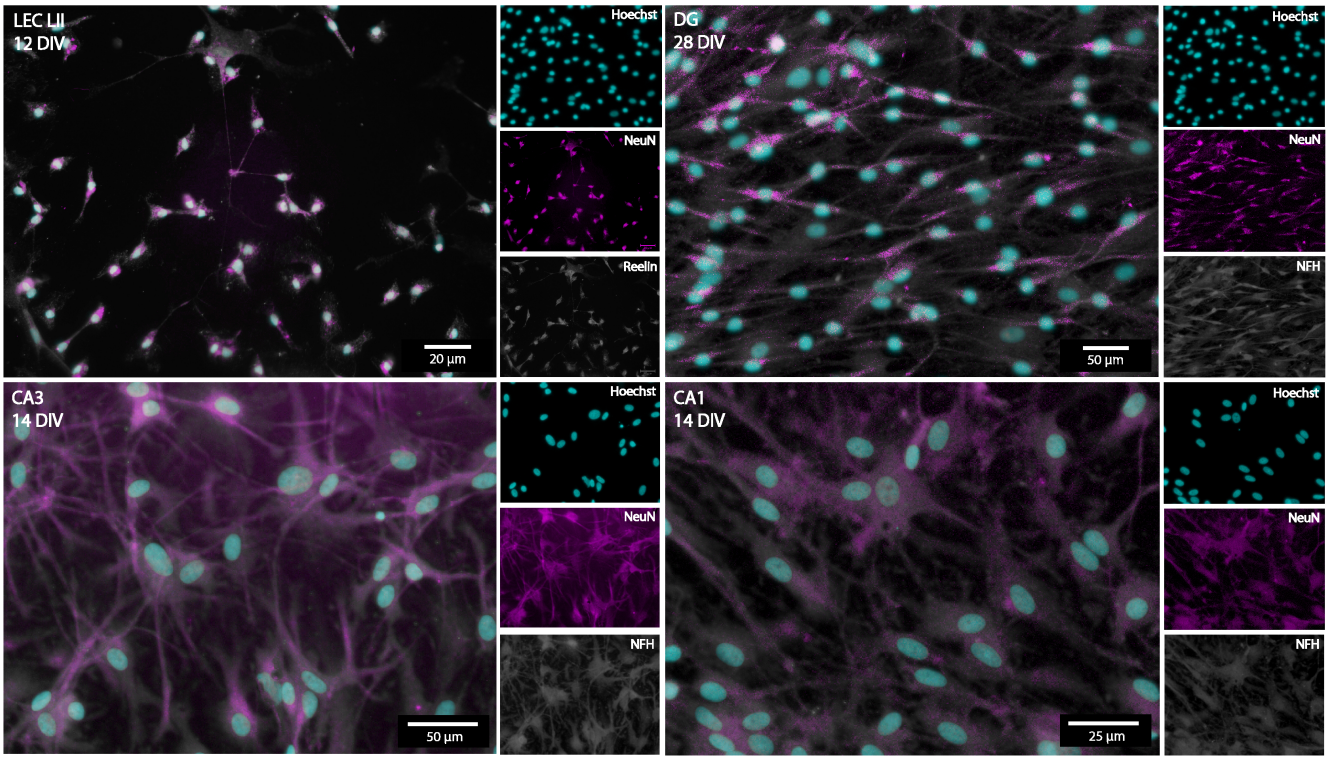

Figure 6 | **Immunocytochemistry of entorhinal-hippocampal AD networks.** Co-expression of the neural marker NeuN and reelin in the LEC LII neurons, and co-expression of NeuN and Neurofilament Heavy for hippocampal DG-gr, CA3-pyr and CA1-pyr confirmed the presence of the neurons of interest.

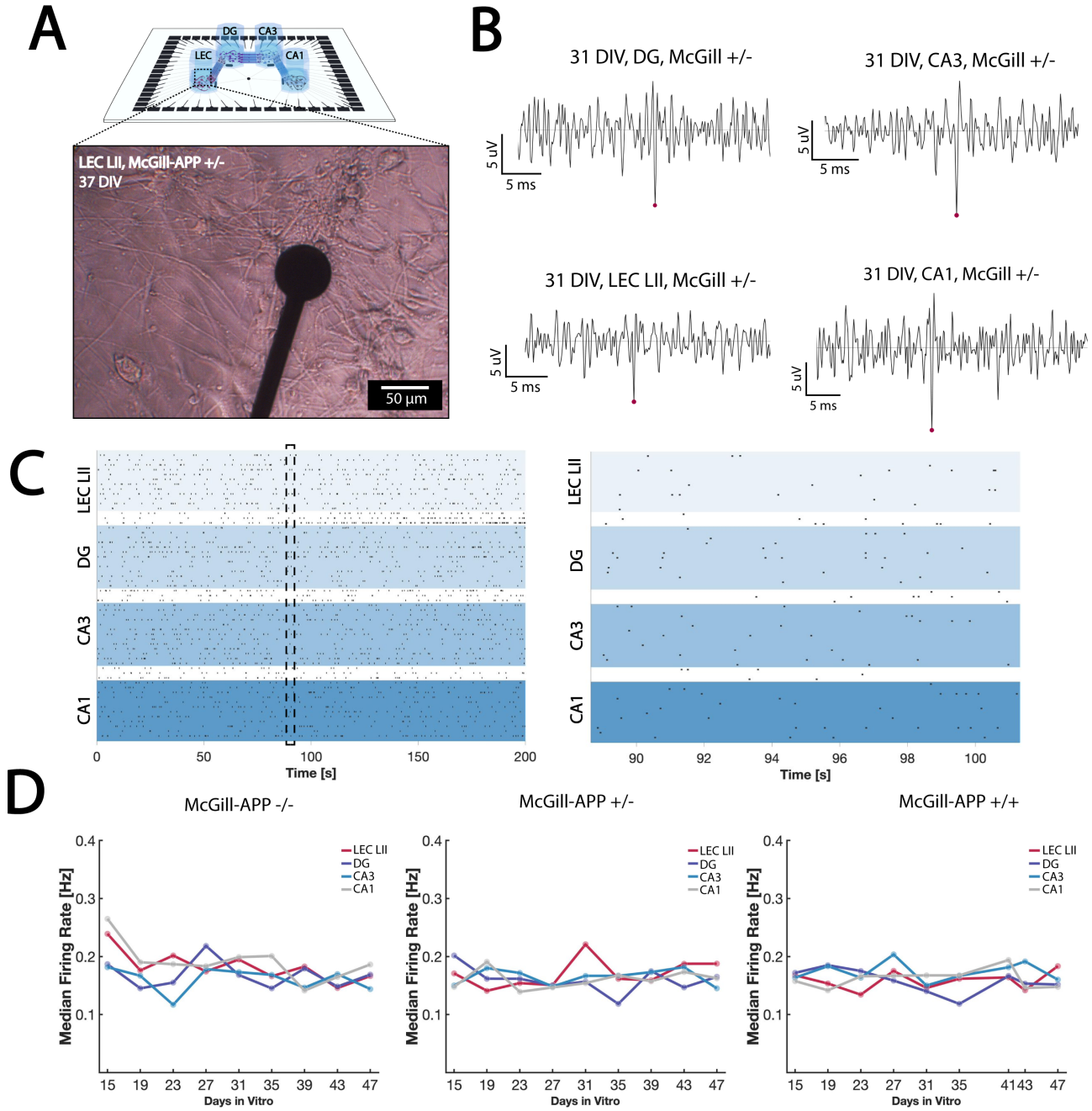

Figure 7 | **Adult entorhinal and hippocampal neural networks from AD-model rats develop sustained electrophysiological activity. (A.)** Illustration of a four-nodal microfluidic chip on a microelectrode array with an inset of a phase contrast image of a lateral entorhinal cortex layer II (LEC LII) neural network derived from a McGill-APP rat +/- (heterozygote genotype). **(B.)** Spike traces showing one representative spike from each subregion, LEC LII (bottom left), DG (top left), CA3 (top right) and CA1 (bottom right) at 31 DIV. **(C.)** Representative raster plots showing spontaneous network activity from all four nodes. One black dot indicates one detected spike. **(D.)** Median firing rate (Hz) over time from 15 DIV up to 47 DIV. LEC LII; Lateral entorhinal cortex layer II. DG; Dentate gyrus. CA3; Cornu ammonis 3. CA1; Cornu ammonis 3. DIV; Days *in vitro*.

Conclusion

In this study, we reverse engineered multinodal cortical-hippocampal neural networks with controllable afferent-efferent connectivity. We validated that both spontaneously evoked and stimulation induced activity propagated in a feed-forward manner between the interconnected nodes in these networks. Interconnection of the multinodal networks contributed to the emergence of complex structure-function dynamics both within and across nodes. This indicates the network´s capacity for both integrated as well as segregated information processing. Furthermore, long-term culturing of adult entorhinal-hippocampal network from AD model animals demonstrate the wide potential of this advanced modelling approach. These neurons self-organize, re-form structural connections and demonstrate spontaneous electrophysiologically activity. Thus, this reverse engineering approach presents a significant step towards modelling anatomically relevant neural networks in different configurations for pre-clinical disease modelling.

AUTHOR CONTRIBUTIONS

The author contributions follow the CRediT system. **KSH**: Conceptualization, Methodology, Investigation (dissections, cell experiments, electrophysiology, formal analysis), Writing – Original Draft, Visualization. **NWH**: Conceptualization, Methodology, Software, Investigation (chip design & manufacturing, cell experiments, electrophysiology, formal analysis), Writing – Original Draft, Visualization. **SNN**: Investigation (dissections, cell experiments, electrophysiology), Writing – Review & Editing. **IS, AS, MPW, AKF**: Conceptualization, Methodology, Writing – Review & Editing, Funding acquisition, Supervision.

ACKNOWLEDGEMENTS

We would like to thank Hanne Mali Møllegård for breeding of all APP/PS1 mice and Grethe Mari Olsen for breeding of all McGill-R-Thy1-APP rats. NTNU Enabling technologies, The Liaison Committee for education, research and innovation in Central Norway, the Olav Thon Foundation, Samarbeidsorganet HMN-NTNU (23166), K.G. Jebsen Center for Alzheimer's Disease, and Civitan Norwegian Research Fund for Alzheimer's Disease are acknowledged for funding this research. The Research Council of Norway is acknowledged for the support to the Norwegian Micro- and Nano-Fabrication Facility, NorFab, project number 295864. Prof. Michela Chiappalone and Prof. Sergio Martinoia, University of Genova for generously providing the scripts for the Precise Timing Spike Detection algorithm and the logISI burst detection.

COMPETING FINANCIAL INTERESTS

The authors declare that the research was conducted in the absence of any commercial or financial relationships that could be construed as a potential conflict of interest.

Bibliography

1. V. Pasquale, S. Martinoia, and M. Chiappalone. A self-adapting approach for the detection of bursts and network bursts in neuronal cultures. *J. Comput. Neurosci.*, 29:213–29, 2010. doi: 10.1007/s10827-009-0175-1.
2. D. A. Wagenaar, J. Pine, and S. M. Potter. An extremely rich repertoire of bursting patterns during the development of cortical cultures. *BMC Neurosci.*, 7:11, 2006. doi: 10.1186/1471-2202-7-11.
3. M. Chiappalone, M. Bove, A. Vato, M. Tedesco, and S. Martinoia. Dissociated cortical networks show spontaneously correlated activity patterns during in vitro development. *Brain Res.*, 1093(1):41–53, 2006. doi: 10.1016/j.brainres.2006.03.049.
4. A. M. Taylor, S. W. Rhee, C. H. Tu, D. H. Cribbs, C. W. Cotman, and N. L. Jeon. Microfluidic multicompartment device for neuroscience research. *Langmuir*, 19(5):1551–56, 2003. doi: 10.1021/la026417v.
5. A. M. Taylor, M. Blurton-Jones, S. W. Rhee, D. H. Cribbs, C. W. Cotman, and N. L. Jeon. A microfluidic culture platform for cns axonal injury, regeneration and transport. *Nat. Methods*, 2:599–605, 2005. doi: 10.1038/nmeth777.
6. L. Pan, S. Alagapan, E. Franca, S. S. Leondopulos, T. B. DeMarse, G. J. Brewer, and B. C. Wheeler. An in vitro method to manipulate the direction and functional strength between neural populations. *Front. Neural Circuits.*, 9:32, 2015. doi: 10.3389/fncir.2015.00032.
7. T. B. DeMarse, L. Pan, S. Alagapan, G. J. Brewer, and B. C. Wheeler. Feed-forward propagation of temporal and rate information between cortical populations during coherent activation in engineered in vitro networks. *Front. Neural Circuits*, 10, 2016. doi: https://doi.org/10.3389/fncir.2016.00032.
8. V. A. Makarov J. Makarova A. Korovaichuk N. Benito, A. Fernández-Ruiz and O. Herreras. Spatial modules of coherent activity in pathway-specific lfps in the hippocampus reflect topology and different modes of presynaptic synchronization. *Cereb Cortex*, 24(7):1738–52, 2014. doi: 10.1093/cercor/bht022.
9. G. S. Withers, C. D. James, C. E. Kingman, H. G. Craighead, and G. A. Banker. Effects of substrate geometry on growth cone behavior and axon branching. *J. Neurobiol.*, 66: 1183–94, 2006. doi: 10.1002/neu.20298.
10. E. W. Dent, S. L. Gupton, and F. B. Gertler. The growth cone cytoskeleton in axon outgrowth and guidance. *Cold Spring Harb. Perspect. Biol.*, 3(3), 2011. doi: 10.1101/cshperspect.a001800.
11. G. Gangatharan, S. Schneider-Maunoury, and M. A. Breau. Role of mechanical cues in shaping neuronal morphology and connectivity. *Biology of the Cell*, 110(6):125–36, 2018. doi: 10.1111/boc.201800003.
12. J. M. Peyrin, B. Deleglise, L. Saias, M. Vignes, P. Gougis, S. Magnifico, S. Betuing, M. Pietri, J. Caboche, P. Vanhoutte, J. L. Viovy, and B. Brugg. Axon diodes for the reconstruction of oriented neuronal networks in microfluidic chambers. *Lab Chip*, 11(21):3663–73, 2011. doi: 10.1039/c1lc20014c.
13. E. Malishev, A. Pimashkin, A. Gladkov, Y. Pigareva, A. Bukatin, V. Kazantsev, I. Mukhina, and M. Dubina. Microfluidic device for unidirectional axon growth. *Journal of Physics: Conference Series*, 643, 2015. doi: 10.1088/1742-6596/643/1/012025.
14. J. le Feber, W. Postma, E. de Weerd, M. Weusthof, and W. L. Rutten. Barbed channels enhance unidirectional connectivity between neuronal networks cultured on multi electrode arrays. *Front. Neurosci.*, 9:412, 2015. doi: 10.3389/fnins.2015.00412.
15. A. Gladkov, Y. Pigareva, D. Kutyina, V. Kolpakov, A. Bukatin, I. Mukhina, V. Kazantsev, and A. Pimashkin. Design of cultured neuron networks in vitro with predefined connectivity using asymmetric microfluidic channels. *Sci. Rep.*, 7:15625, 2017. doi: 10.1038/s41598-017-15506-2.
16. Y. Pigareva, A. Gladkov, V. Kolpakov, I. Mukhina, A. Bukatin, V. B. Kazantsev, and A. Pimashkin. Experimental platform to study spiking pattern propagation in modular networks in vitro. *Brain Sci.*, 11(6), 2021. doi: 10.3390/brainsci11060717.
17. S. Na, M. Kang, S. Bang, D. Park, J. Kim, S. J. Sim, S. Chang, and N. L. Jeon. Microfluidic neural axon diode. *Technology*, 4(4):240–8, 2016. doi: https://doi.org/10.1142/S2339547816500102.
18. P. M. Holloway, G. I. Hallinan, M. Hegde, S. I. R. Lane, K. Deinhardt, and J. West. Asymmetric confinement for defining outgrowth directionality. *Lab Chip*, 19(8):1484–89, 2019. doi: 10.1039/c9lc00078j.
19. R. Renault, J. B. Durand, J. L. Viovy, and C. Villard. Asymmetric axonal edge guidance: a new paradigm for building oriented neuronal networks. *Lab Chip*, 16(12):2188–91, 2016. doi: 10.1039/c6lc00479b.
20. N. Winter-Hjelm, Å. B. Tomren, P. Sikorski, A. Sandvig, and I. Sandvig. Structure-function dynamics of engineered, modular neuronal networks with controllable afferent-efferent connectivity. *bioRxiv*, 2022. doi: https://doi.org/10.1101/2022.11.24.517848.
21. Y. S. Vakilna, W. C. Tang, B. C. Wheeler, and G. J. Brewer. The flow of axonal information among hippocampal subregions: 1. feed-forward and feedback network spatial dynamics underpinning emergent information processing. *Front. Neural Circuits*, 15, 2021. doi: https://doi.org/10.3389/fncir.2021.660837.
22. H. Yamamoto, S. Moriya, K. Ide, T. Hayakawa, H. Akima, S. Sato, S. Kubota, T. Tanii, M. Niwano, S. Teller, J. Soriano, and A. Hirano-Iwata. Impact of modular organization on dynamical richness in cortical networks. *Sci. Adv.*, 4(1), 2018. doi: 10.1126/sciadv.aau4914.
23. M. U. Park, Y. Bae, K.-S. Lee, J. H. Song, S. M. Lee, and K.-H. Yoo. Collective dynamics of neuronal activities in various modular networks. *Lab Chip*, 21:951—-61, 2021. doi: 10.1039/d0lc01106a.
24. R. van de Wijdeven, O. H. Ramstad, U. S. Bauer, Ø. Halaas, A. Sandvig, and I. Sandvig. Structuring a multi-nodal neural network in vitro within a novel design microfluidic chip. *Biomed. Microdevices*, 20:9, 2018. doi: 10.1007/s10544-017-0254-4.
25. B. J. Dworak and B. C. Wheeler. Novel mea platform with pdms microtunnels enables the detection of action potential propagation from isolated axons in culture. *Lab Chip*, 9(3): 404–10, 2009. doi: 10.1039/b806689b.
26. I. Baruchi, V. Volman, N Raichman, M. Shein, and E. Ben-Jacob. The emergence and properties of mutual synchronizationinin vitrocoupled cortical networks. *Eur. J. Neurosci.*, 28(9):1825–35, 2008. doi: 10.1111/j.1460-9568.2008.06487.x.
27. M. Shein-Idelson, G. Cohen, E. Ben-Jacob, and Y. Hanein. Modularity induced gating and delays in neuronal networks. *PLoS Comput. Biol.*, 12(4):e1004883, 2016. doi: 10.1371/journal.pcbi.1004883.
28. N. M. van Strien, N. L. Cappaert, and M. P. Witter. The anatomy of memory: an interactive overview of the parahippocampal-hippocampal network. *Nat Rev Neurosci*, 10(4):272–82, 2009. ISSN 1471-003x. doi: 10.1038/nrn2614. 1471-0048 van Strien, N M Cappaert, N L M Witter, M P Journal Article Review England 2009/03/21 Cell Adhesion/physiology Cell Communication/*physiology Humans Memory/*physiology Nerve Net/*physiology.
29. H. Braak and E. Braak. Neuropathological stageing of alzheimer-related changes. *Acta Neuropathol*, 82(4):239–259, 1991. doi: 10.1007/bf00308809.
30. D. R. Thal, U. Rüb, M. Orantes, and H. Braak. Phases of a beta-deposition in the human brain and its relevance for the development of ad. *Neurology*, 58(12):1791–800, 2002. doi: https://doi.org/10.1212/wnl.58.12.1791.
31. K.A. Vossel, Beagle A. J., H. Rabinovivi, S. E. Shu, E. Lee, and G. et al. Naasan. Seizures and epileptiform activity in the early stages of alzheimer disease. *JAMA Neurol*, 70(9): 1158–66, 2013. doi: https://doi.org/10.1001/jamaneurol.2013.136.
32. D. W. McKeel Jr. J. C. Morris J. H. Growdon T. Gomez-Isla, J. L. Price and B. T. Hyman. Profound loss of layer ii entorhinal cortex neurons occurs in very mild alzheimer's disease. *J Neurosci*, 16(14):491–500, 1996. doi: PMCID:PMC6578866.
33. G. T. Stebbins S. T. DeKosky E. J. Cochran D. Bennett et al. J. H. Kordower, Y. Chu. Loss and atrophy of layer ii entorhinal cortex neurons in elderly people with mild cognitive impairment. *Ann Neurol*, 49(2):202–213, 2001. doi: PMID:11220740.
34. F. A. Schmitt S. W. Scheff, D. A. Price and E. J. Mufson. Hippocampal synaptic loss in early alzheimer's disease and mild cognitive impairment. *Neurobiol Aging*, 27(6), 2006. doi: 10.1016/j.neurobiolaging.2005.09.012.
35. F. A. Schmitt S. T. DeKosky S. W. Scheff, D. A. Price and E. J. Mufson. Synaptic alterations in ca1 in mild alzheimer disease and mild cognitive impairment. *Neurology*, 68(18):1501–8,

2007. doi: 10.1212/01.wnl.0000260698.46517.8f.
36. Y. Dong and G. J. Brewer. Global metabolic shifts in age and alzheimer's disease mouse brains pivot at nad+/nadh redox sites. *J Alzheimers Dis*, 71(1):119–140, 2019. ISSN 1387-2877 (Print) 1387-2877. doi: 10.3233/jad-190408.
37. Y. Dong, S. Sameni, M. A. Digman, and G. J. Brewer. Reversibility of age-related oxidized free nadh redox states in alzheimer's disease neurons by imposed external cys/cyss redox shifts. *Sci Rep*, 9(1):11274, 2019. ISSN 2045-2322. doi: 10.1038/s41598-019-47582-x.
38. Y. Dong, M. A. Digman, and G. J. Brewer. Age- and ad-related redox state of nadh in subcellular compartments by fluorescence lifetime imaging microscopy. *Geroscience*, 41 (1):51–67, 2019. ISSN 2509-2715 (Print) 2509-2723. doi: 10.1007/s11357-019-00052-8.
39. K. S Hanssen, M. P. Witter, A., I. Sandvig, and A. Kobro-Flatmoen. Dissection and culturing of adult lateral entorhinal cortex layer ii neurons from app/ps1 alzheimer model mice. *J. Neurosci. Methods*, 390, 2023. doi: https://doi.org/10.1016/j.jneumeth.2023.109840.
40. A. Ahluwalia S. Alam M. T. Avey M. Baker et al. N. Percie du Sert, V. Hurst. The arrive guidelines 2.0: Updated guidelines for reporting animal research. *PLoS Biol*, 18(7):e3000410, 2020.
41. R. Radde, T. Bolmont, S. A. Kaeser, J. Coomaraswamy, D. Lindau, L. Stoltze, M. E. Calhoun, F. Jäggi, H. Wolburg, S. Gengler, C. Haass, B. Ghetti, C. Czech, C. Hölscher, P. M. Mathews, and M. Jucker. Abeta42-driven cerebral amyloidosis in transgenic mice reveals early and robust pathology. *EMBO Rep*, 7(9):940–6, 2006. ISSN 1469-221X (Print) 1469-221x. doi: 10.1038/sj.embor.7400784.
42. V. Partridge S. Allard M. T. Ferretti A. DeWilde et al. W. C. Leon, F. Canneva. A novel transgenic rat model with a full alzheimer's-like amyloid pathology displays pre-plaque intracellular amyloid-beta-associated cognitive impairment. *J Alzheimers Dis*, 20(1):113–26, 2010. doi: 10.3233/jad-2010-1349.
43. A. Nagelhus A. Kobro-Flatmoen and M. P. Witter. Reelin-immunoreactive neurons in entorhinal cortex layer ii selectively express intracellular amyloid in early alzheimer's disease. *Neruobiol Dis*, 93:172–83, 2016. doi: 10.1016/j.nbd.2016.05.012.
44. P. Kvello I. Heggland and M. P. Witter. Electrophysiological characterization of networks and single cells in the hippocampal region of a transgenic rat model of alzheimer's disease. *eNeuro*, 6(1), 2019. doi: 10.1523/eneuro.0448-17.2019.
45. D. Waters S. E. Counts S. E. Perez S. T. DeKosky et al. E. J. Mufson, L. Mahady. *Neuroscience*, 309:51–67, 2015. doi: 10.1016/j.neuroscience.2015.03.006.
46. G. W. Van Hoesen B. T. Hyman and A. R. Damasio. Alzheimer's disease: glutamate depletion in the hippocampal perforant pathway zone. *Ann Neurol*, 22(1):37–40, 1987. doi: 10.1002/ana.410220110.
47. K. N. Richter, N. H. Revelo, K. J. Seitz, M. S. Helm, D. Sarkar, R. S. Saleeb, E. D'Este, J. Eberle, E. Wagner, C. Vogl, D. F. Lazaro, F. Richter, J. Coy-Vergara, G. Coceano, E. S. Boyden, R. R. Duncan, S. W. Hell, M. A. Lauterbach, S. E. Lehnart, T. Moser, T. F. Outeiro, P. Rehling, B. Schwappach, I. Testa, B. Zapiec, and S. O. Rizzoli. Glyoxal as an alternative fixative to formaldehyde in immunostaining and super-resolution microscopy. *EMBO J.*, 37: 139–59, 2018. doi: 10.15252/embj.201695709.
48. J. C. Lansey. Beautiful and distinguishable line colors + colormap, 2022.
49. C. A. Brewer, G. W. Hatchard, and M. A. Harrower. Colorbrewer in print: A catalog of color schemes for maps. *Cartography and Geographic Information Science*, 30(1):5–32, 2003. doi: https://doi.org/10.1559/152304003100010929.
50. A. Maccione, M. Gandolfo, P. Massobrio, A. Novellino, S. Martinoia, and M. Chiappalone. A novel algorithm for precise identification of spikes in extracellularly recorded neuronal signals. *J. Neurosci. Methods*, 177(1):241–9, 2009. doi: 10.1016/j.jneumeth.2008.09.026.
51. B. Kraus. Spike raster plot, 2022.
52. L. L. Bologna, V. Pasquale, M. Garofalo, M. Gandolfo, P. L. Baljon, A. Maccione, S. Martinoia, and M. Chiappalone. Investigating neuronal activity by spycode multi-channel data analyzer. *Neural Networks*, 23(6):685–97, 2010. doi: 10.1016/j.neunet.2010.05.002.
53. M. Rubinov and O. Sporns. Complex network measures of brain connectivity: uses and interpretations. *NeuroImage*, 52(3):1059–69, 2010. doi: 10.1016/j.neuroimage.2009.10.003.
54. V. D. Blondel, J. L. Guillaume, R. Lambiotte, and E. Lefebvre. Fast unfolding of communities in large networks. *J. Stat. Mech. Theory Exp.*, 2008:P10008, 2008. doi: 10.1088/1742-5468/2008/10/P10008.
55. D. A. Wagenaar and S. M. Potter. Real-time multi-channel stimulus artifact suppression by local curve fitting. *J. Neurosci. Methods*, 120(2):113–20, 2002. doi: 10.1016/s0165-0270(02)00149-8.
56. J. S. Weir, N. Christiansen, A. Sandvig, and I. Sandvig. Selective inhibition of excitatory synaptic transmission alters the emergent bursting dynamics of in vitro neural networks. *Front. Neural Circuits*, 2023. doi: 10.3389/fncir.2023.1020487.
57. K. Heiney, O. H. Ramstad, V. Fiskum, A. Sandvig, A. Sandvig, and S. Nichele. Neuronal avalanche dynamics and functional connectivity elucidate information propagation in vitro. *Front. Neural Circuits*, 16, 2022. doi: https://doi.org/10.3389/fncir.2022.980631.
58. J. Nunez. Differential expression of microtubule components during brain development. *Dev. Neurosci.*, 8(3):125–41, 1986. doi: https://doi.org/10.1159/000112248.
59. R. P. Tucker. The roles of microtubule-associated proteins in brain morphogenesis: a review. *Brain Res. Rev.*, 15(2):101–20, 1990. doi: https://doi.org/10.1016/0165-0173(90)90013-E.
60. A. Matus. Microtubule-associated proteins and neuronal morphogenesis. *J. Cell Sci.*, 15: 61–7, 1991. doi: https://doi.org/10.1242/jcs.1991.Supplement_15.9.
61. G. V. W. Johnson and R. S. Jope. The role of microtubule-associated protein 2 (map-2) in neuronal growth, plasticity, and degeneration. *J. Neurosci. Res.*, 33(4):505–12, 1992. doi: https://doi.org/10.1002/jnr.490330402.
62. M. A. Tischfield, H. N. Baris, C. Wu, G. Rudolph, L. Van Maldergem, W. He, W.-M. Chan, C. Andrews, J. L. Demer, R. L. Robertson, D. A. Mackey, J. B. Ruddle, T. D. Bird, I. Gottlob, C. Pieh, E. Traboulsi, S. L. Pomeroy, D. G. Hunter, J. S. Soul, A. Newlin, L. J. Sabol, E. J. Doherty, C. E. de Uzcátegui, N. de Uzcátegui, M. L. Z. Collins, E. C. Sener, B. Wabbels, H. Hellebrand, T. Meitinger, T. de Berardinis, A. Magli, C. Schiavi, M. Pastore-Trossello, F. Koc, A. M. Wong, A. V. Levin, M. T. Geraghty, M. Descartes, M. Flaherty, R. V. Jamieson, H. U. Møller, I. Meuthen, D. F. Callen, J. Kerwin, S. Lindsay, A. Meindl, M. L. Gupta, D. Pellman, and E. C. Engle. Human tubb3 mutations perturb microtubule dynamics, kinesin interactions, and axon guidance. *Cell*, 140(1):74–87, 2010. doi: https://doi.org/10.1016/j.cell.2009.12.011.
63. A. B. Oestreicher, P. N. E. De Graan, W. H. Gispen, J. Verhaagen, and L. H. Schrama. B-50, the growth associated protein-43: modulation of cell morphology and communication in the nervous system. *Prog. Neurobiol.*, 53(6):627–86, 1997. doi: https://doi.org/10.1016/S0301-0082(97)00043-9.
64. R. J. Mullen, C. R. Buck, and A. M. Smith. Neun, a neuronal specific nuclear protein in vertebrates. *J. Dev.*, 116(1):201–11, 1992. doi: https://doi.org/10.1242/dev.116.1.201.
65. W. W. Schlaepfer and J. Bruce. Simultaneous up-regulation of neurofilament proteins during the postnatal development of the rat nervous system. *J. Neurosci. Res.*, 25(1):39–49, 1990. doi: https://doi.org/10.1002/jnr.490250106.
66. L. F. Eng, R. S. Ghirnikar, and Y. L. Lee. Glial fibrillary acidic protein: Gfap-thirty-one years (1969–2000). *Neurochem. Res.*, 25:1439–51, 2000. doi: https://doi.org/10.1023/A:1007677003387.
67. M. Shanahan. Dynamical complexity in small-world networks of spiking neurons. *Phys. Rev. E.*, 78(4), 2008. doi: https://doi.org/10.1103/PhysRevE.78.041924.
68. M. Rubinov, O. Sporns, J.-P. Thivierge, and M. Breakspear. Neurobiologically realistic determinants of self-organized criticality in networks of spiking neurons. *PLoS Comput. Biol.*, 7(6):e1002038, 2011. doi: https://doi.org/10.1371/journal.pcbi.1002038.
69. D. Meunier, R. Lambiotte, and E. T. Bullmore. Modular and hierarchically modular organization of brain networks. *Front. Neurosci.*, 4(200), 2010. doi: https://doi.org/10.3389/fnins.2010.00200.
70. M. A. Collings M. S. Evans and G. J. Brewer. Electrophysiology of embryonic, adult and aged rat hippocampal neurons in serum-free culture. *J Neurosci Methods*, 79(1):37–46, 1998. doi: 10.1016/s0165-0270(97)00159-3.
71. N. Bhargava M. Stancescu P. Molnar M. S. Kindy et al. K. Varghese, M. Das. Regeneration and characterization of adult mouse hippocampal neurons in a defined in vitro system. *J Neurosci Methods*, 177(1):51–9, 2009. doi: 10.1016/j.jneumeth.2008.09.022.
72. C. Marques de Freria K. Groeniger M. C. Marchetto S. Dupraz et al. E. A. van Niekerk, R. Kawaguchi. Methods for culturing adult cns neurons reveal a cns conditioning effect. *Cell Rep Methods*, 2(7):100255, 2022. doi: 10.1016/j.crmeth.2022.100255.
73. E. S. Nilssen, B. Jacobsen, G. Fjeld, R. R. Nair, S. Blankvoort, C. Kentros, and M. P. Witter. Inhibitory connectivity dominates the fan cell network in layer ii of lateral entorhinal cortex. *J Neurosci*, 38(45):9712–9727, 2018. ISSN 0270-6474 (Print) 0270-6474. doi: 10.1523/jneurosci.1290-18.2018.
74. H. A. Henning J. Reichwald M. Staufenbiel B. Sakmann et al. M. A. Busche, X. Chen. Critical role of soluble amyloid-β for early hippocampal hyperactivity in a mouse model of alzheimer's disease. *Proc Natl Acad Sci*, 109(22):8740–5, 2012. doi: 10.1073/pnas.1206171109.
75. E. Carbone A. Marcantoni, E. F. Raymond and H. Marie. Firing properties of entorhinal cortex neurons and early alterations in an alzheimer's disease transgenic model. *Pflugers Arch*, 466(7):1437–50, 2014. doi: 10.1007/s00424-013-1368-z.
76. VD. Valderhaug, OH. Ramstad, R. van de Wijdeven, K. Heiney, S. Nichele, A. Sandvig, and I Sandvig. Structural and functional alterations associated with the lrrk2 g2019s mutation revealed in structured human neural networks. *bioRxiv*, 2021. doi: https://doi.org/10.1101/2020.05.02.073726.
77. A. Bhattacharya, H. Desai, T. B. DeMarse, B. C. Wheeler, and G. J. Brewer. Repeating spatial-temporal motifs of ca3 activity dependent on engineered inputs from dentate gyrus neurons in live hippocampal networks. *Front. Neural Circuits*, 10, 2016. doi: https://doi.org/10.3389/fncir.2016.00045.
78. D. Poli, S. Thiagarajan, T. B. DeMarse, B. C. Wheeler, and G. J. Brewer. Sparse and specific coding during information transmission between co-cultured dentate gyrus and ca3 hippocampal networks. *Front. Neural Circuits*, 11, 2017. doi: https://doi.org/10.3389/fncir.2017.00013.
79. D. Poli, B. C. Wheeler, T. B. DeMarse, and G. J. Brewer. Pattern separation and completion of distinct axonal inputs transmitted via micro-tunnels between co-cultured hippocampal dentate, ca3, ca1 and entorhinal cortex networks. *J. Neural Eng.*, 15, 2018. doi: 10.1088/1741-2552/aabc20.

Supplementary Materials

Table S1 | Overview of media supplement compositions in different protocols used throughout the study.

Protocol 1	Protocol 2	Protocol 3	Protocol 4	Protocol 5	Protocol 6
NPM	NPM	NPM	NPM	NPM	NPM
0.2 % B27+	0.2 % B27+	0.2 % B27+	0.2 % B27+	0.2 % B27+	0.2 % B27+
0.025 GlutaMAX	0.025 GlutaMAX	0.025 GlutaMAX	0.025 GlutaMAX	0.025 GlutaMAX	0.025 GlutaMAX
0.001 % BDNF	5 ng/mL FGF2	10 ng/mL FGF2	10 ng/mL FGF2	0.001 % BDNF	10 ng/mL FGF2
0.01 % Penstrep	0.01 % Penstrep	0.01 % Penstrep	10 ug/mL Gentamycin	0.01 % Penstrep	0.01 % Penstrep
0.001 % RI	0.001 % RI	0.001 % RI	0.00 % RI	0.001 % RI	0.001 % RI
0.1 % FBS	0.1 % FBS	0.1 % FBS	0.0 % FBS	0.1 % FBS	0.1 % FBS

NPM; Neurobasal Plus Medium (Thermo Fischer Scientific. B27+; B27 Plus Supplement (Thermo Fischer Scientidic). BDNF; Brain Derived Neurotrophic Factor (Thermo, Catnr). FGF2; F Growth Factor 2 (Thermo, Catnr). PS; Penicillin-Streptomycin (Catnr, Prod). GlutaMAX Supplement (Prod, Catnr). RI; Rock Inhibitor (Prod, catnr). FBS; Fetal Bovine Serum (Prod, catnr).

Table S2 | Overview of animals in the study.

Animal model	Number	Sex	Age	Genotype
McGill-R-Thy1-APP rat	5	M	P38-P89	Heterozygote +/-
McGill-R-Thy1-APP rat	4	M	P46-P53	Homozygote -/-
McGill-R-Thy1-APP rat	12	M	P43-P78	Homozygote +/+
McGill-R-Thy1-APP rat	14	F	P39-P81	Heterozygote +/-
McGill-R-Thy1-APP rat	1	F	P53	Homozygote -/-
McGill-R-Thy1-APP rat	7	F	P37-P72	Homozygote +/+
APP/PS1 mouse	2	F	P79-P80	APP/PS1 +/-

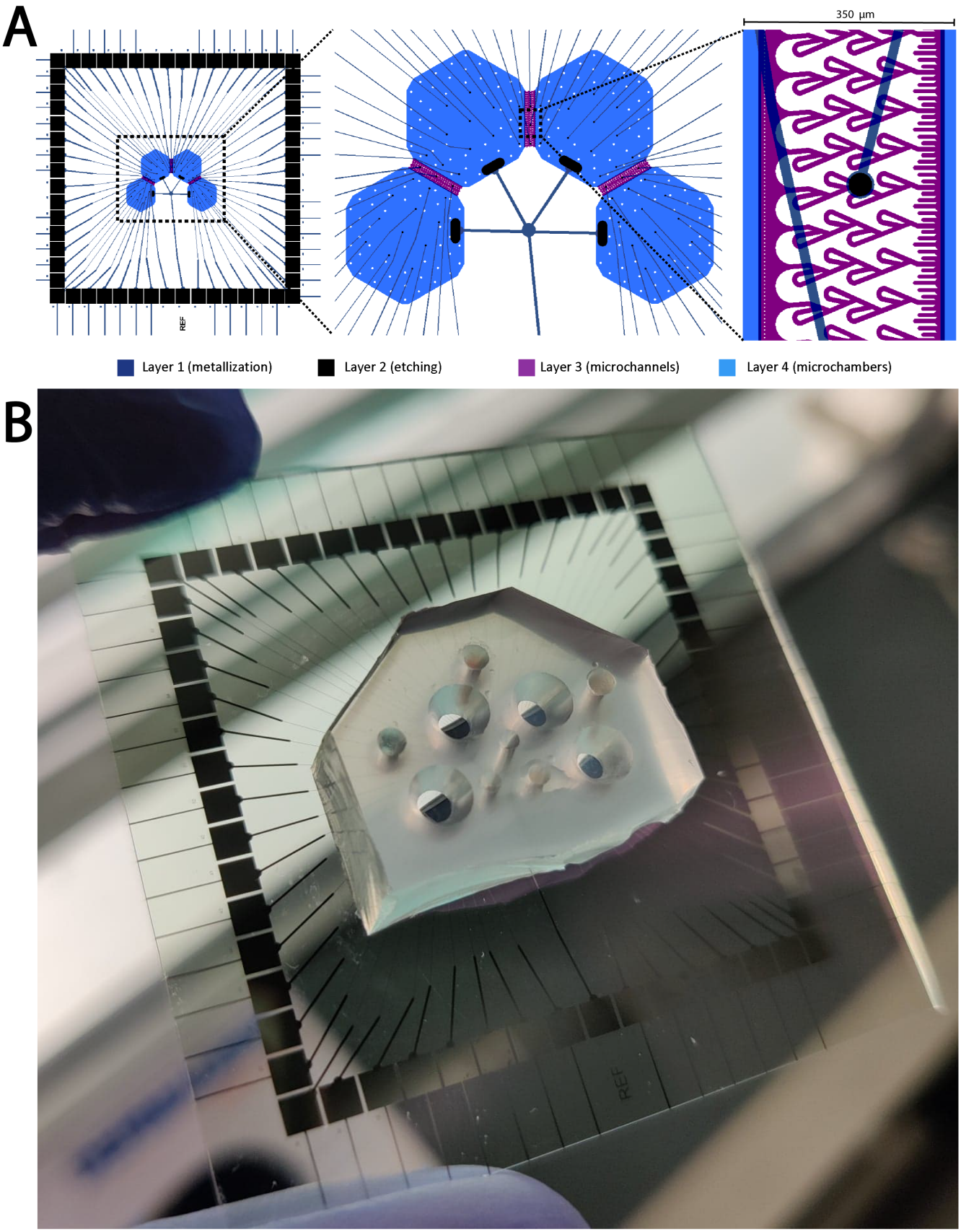

Figure S1 | **CAD design of the Microfluidic MEAs. (A.)** The microfluidic design with $350\,\mu\mathrm{m}$ Tesla-valve channels. Layer 1 represents the design for the metallization (i.e. forming the microelectrodes and corresponding contact pads), layer 2 the etch mask for etching through the passivation layer, layer 3 the mold for the microfluidic channels and layer 4 the mold for the cell compartments. **(B.)** A four-nodal microfluidic chip interfaced with a MEA.

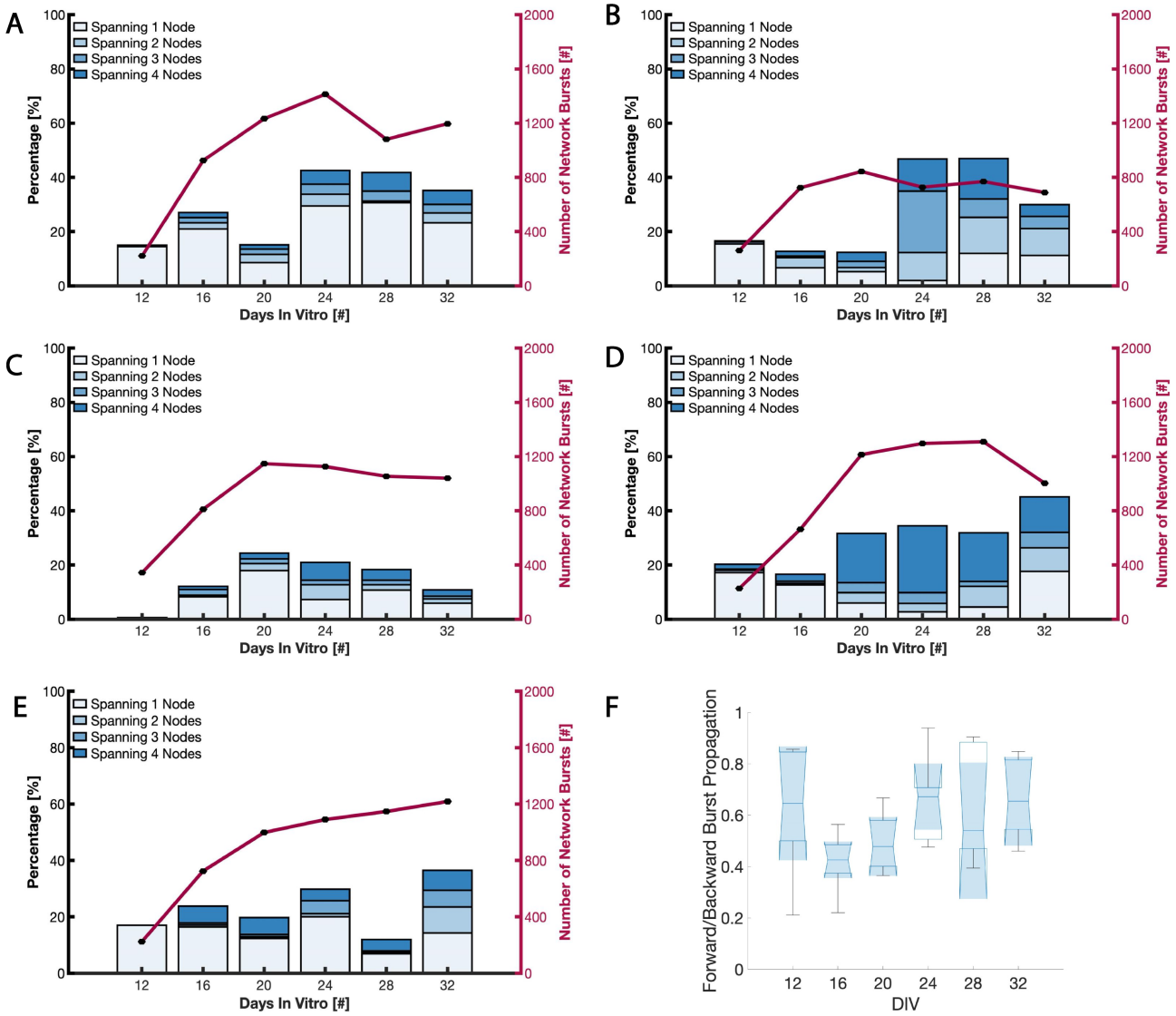

Figure S2 | **Network bursts spread through an increasing number of nodes with time. (A.-B.)** Histograms showing the percentage of spontaneously evoked network bursts initiated within the cortical population, and the number of nodes they span. Each subfigure represents the activity from a single MEA. The total number of network bursts initiated at each DIV is shown along the secondary y-axis. **(F.)** Box plot showing the fraction of bursts propagating in the forward versus backward direction between the four nodes.

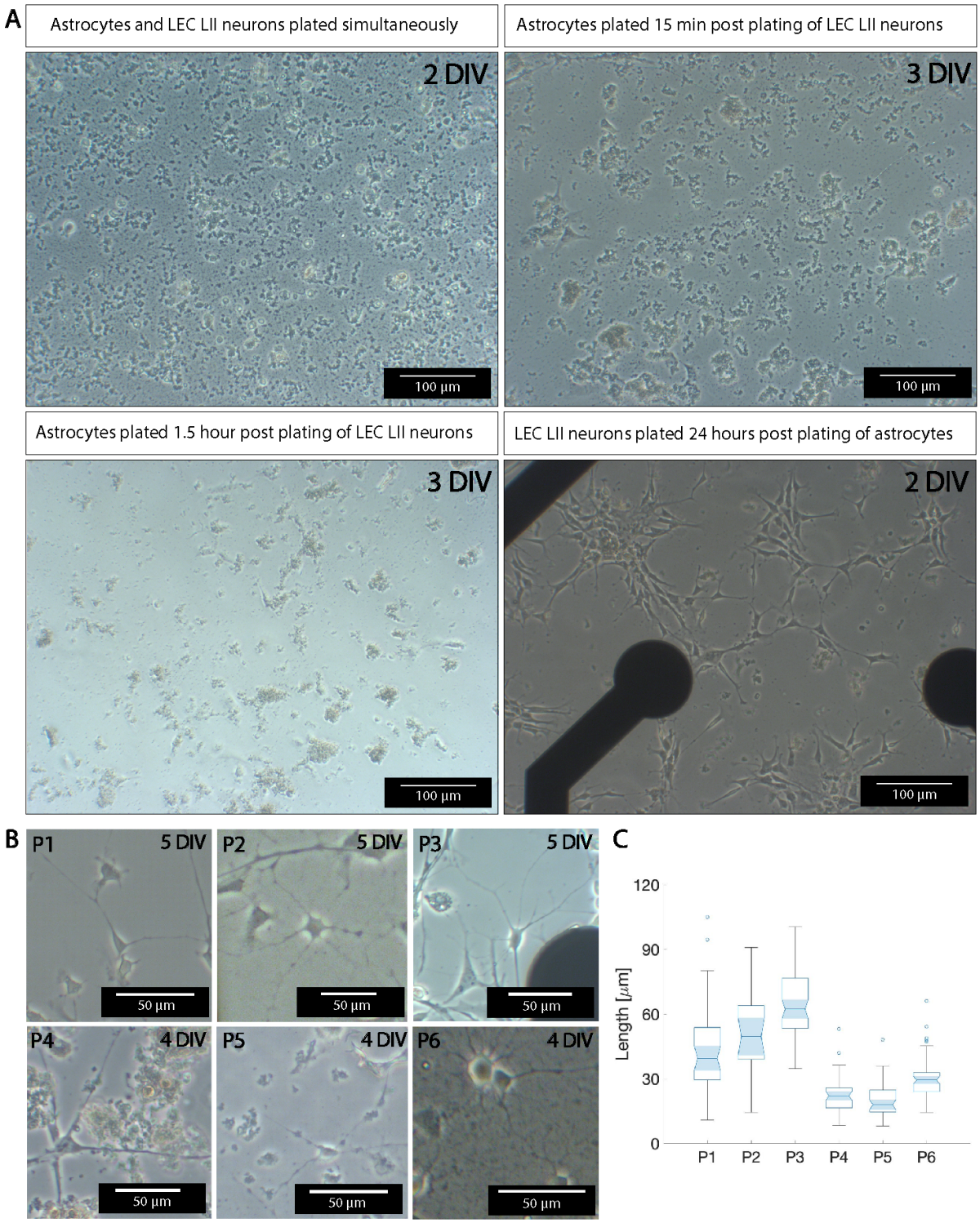

Figure S3 | **Importance of an astrocytic monolayer and media supplement combination. (A.)** Phase contrast images of astrocytes and LEC LII neurons plated simultaneously (top left), astrocytes plated 15 min post plating of LEC LII neurons (top right), astrocytes plated 1.5 hour post plating of LEC LII neurons (bottom left) and LEC LII neurons plated 24 hours post plating of astrocytes (bottom right). **(B.)** Phase contrast images of cultured neurons on six different media supplement protocols and a bar graph showing the mean neurite length for each culture at 5 or 4 DIV. A total of 285 neurites were measured.

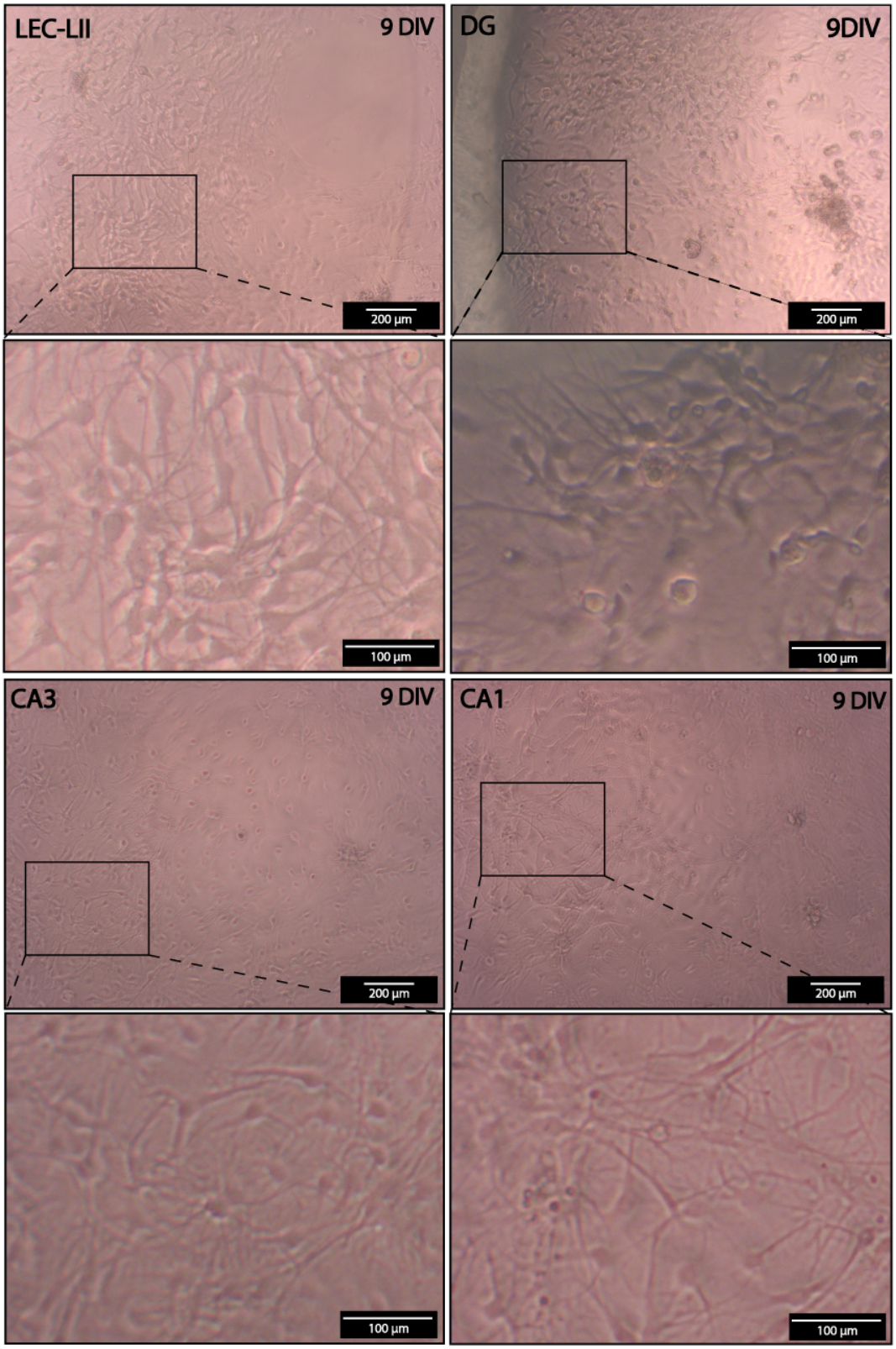

Figure S4 | **Adult mouse neurons reform structural connections in vitro.** Phase-contrast images of adult neurons from the APP/PS1 mouse model at 9 DIV. LEC LII; lateral entorhinal cortex layer II. DG; dentage gyrus. CA3/CA1; cornu ammonis 3/1. DIV; days in vitro.

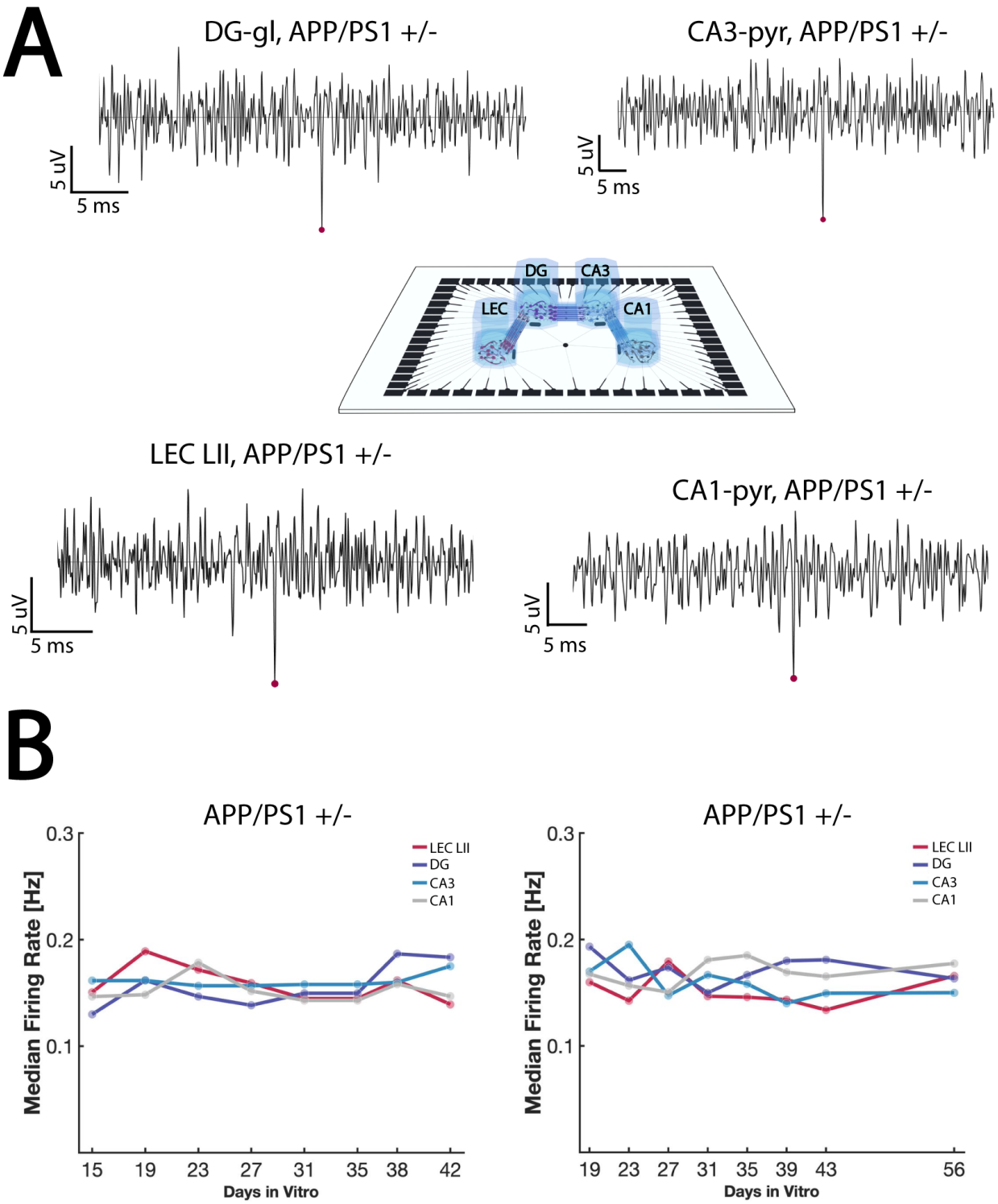

Figure S5 | **Adult mouse neurons obtain electrophysiological activity in vitro. (A.)** Simplified figure of the 4-nodal mMEA with spike traces showing one detected spike from each region (LEC LII, DG, CA3 and CA1. **(B.)** Graph of median firing rate (Hz) from 15 to 42 DIV (left) and 15 to 56 DIV (right). mMEA; microfluidic microelectrode array. LEC LII; lateral entorhinal cortex layer II. DG-gr; dentate gyrus granular. CA3-pyr/CA1-pyr; Cornu ammonis 1/3 pyramidal).